CHALMERS
UNIVERSITY OF TECHNOLOGY

Analysis of Enhanced Heat Transfer in Corrugated Tubes

Master's Thesis in the Sustainable Energy Systems programme

Robert Palm

Department of Chemistry and Chemical Engineering
Chalmers University of Technology
Gothenburg, Sweden 2016

MASTER'S THESIS

Analysis of Enhanced Heat Transfer in Corrugated Tubes

Masters Thesis within the Sustainable Energy Systems programme

ROBERT PALM

SUPERVISOR:

Ronnie Andersson

EXAMINER

Ronnie Andersson

Department of Chemistry and Chemical Engineering
CHALMERS UNIVERSITY OF TECHNOLOGY

Gothenburg, Sweden 2016

Analysis of Enhanced Heat Transfer in Corrugated Tubes
Masters Thesis within the Sustainable Energy Systems programme
Robert Palm

Department of Chemistry and Chemical Engineering
Chalmers University of Technology
SE-412 96 Gothenburg
Sweden
Telephone: + 46 (0)31-772 1000

Chalmers Reproservice
Gothenburg, Sweden 2016

Analysis of Enhanced Heat Transfer in Corrugated Tubes
Robert Palm
Department of Chemistry and Chemical Engineering
Chalmers University of Technology

ABSTRACT

Several methods of enhancing heat transfer performance by introducing disturbances in tubes exist, these disrupts the thermal boundary layer and thus, increases heat transfer rate. This is also accompanied by increased pressure drop due to the increased hindrance of the flow. In this work heat transfer enhancement is investigated using large eddy simulations by introducing internal corrugations in a tube with internal diameter of 5 cm and flow characteristics of 20000 in Reynolds number. The aim was to learn more how the boundary layers are affected by the corrugations and how the enhanced heat transfer is sustained until it is decreased and further disturbances need to be introduced. The simulations were done for a smooth tube and three different rough tube designs, where the pitch (p) to roughness height (e) ratio was varied from 2.2, 10 and 20 for the respective cases. For each simulation the heat and momentum transfer is quantified in the form of Nusselt number and pressure drop which were compared with empirical correlations. The simulations were of good LES quality, where the smooth and p/e = 2.2 design were in good agreement with correlations, in comparison to 10 and 20 where lack of correlations was apparent. The heat transfer performance was increased around 200 % for all the rough tube designs but had a maximum at p/e = 10 where it was enhanced by around 218 %. The pressure drop did not increase in the same way as p/e = 2.2 yielded the lowest pressure drop and p/e = 10 the highest. Thus in terms of operational costs the p/e = 2.2 case yields the highest heat transfer enhancement in relation to pressure drop as it yields an increase in heat transfer performance comparable to p/e = 10 but has a pressure drop only a factor of 3.44 larger than the smooth case, instead of 7.62 as for p/e = 10. It was further seen that the enhanced heat transfer starts to decrease close the next corrugation for p/e = 10 and earlier for p/e = 20 where the boundary layer thickness starts to increase after one third of the distance between the corrugations and thus reducing the heat transfer. It could be concluded that the "general" wall functions for the smooth and rough (densely packed) case is Reynolds dependant as the LES data does not collapse on the wall function. Furthermore the velocity and temperature profiles in the near wall region are strongly dependent on the separation of the corrugations, and further dependent on the post-processing method.

Keywords: CFD, LES, heat transfer, corrugation, boundary layer

ACKNOWLEDGEMENTS

I would like to thank my supervisor and examiner, Assoc. Prof. Ronnie Andersson, first of all for giving me the opportunity to perform this project. Further I appreciate the support and discussions during the project, which has given me valuable insight in heat transfer, turbulence and simulations. I would also like to thank PhD Olle Högblom and Lic. Eng. Soheil Soltani for guidance in meshing and general discussions. Finally I would like to thank my fellow thesis workers and the people at the department for a great time.

Contents

NOTATIONS

Roman letters

B	intersection constant, see Eq. 2.48
B_T	intersection constant, see Eq. 2.50
c_P	specific heat capacity at constant pressure, $[J/kg\ K]$
D	tube diameter
e	roughness height, $[m]$
k	roughness height, $[m]$
k^+	dimensionless roughness height, [-]
Nu	Nusselt number, [-]
P	pressure, [Pa]
Pr	Prandtl number, [-]
q	wall heat flux, $[W/m^2]$
Re	Reynolds number, [-]
T	temperature, $[K]$
T_w	wall temperature, $[K]$
T^+	dimensionless temperature, [-]
u_τ	friction velocity, $[m/s]$, see Eq. 2.40
U	velocity, $[m/s]$
U^+	dimensionless velocity, [-]
y	distance from the wall, $[m]$
y^+	dimensionless distance from the wall, [-]

Greek letters

β	linearly-varying component of pressure, see Eq. 2.38
θ	temperature scaling function, see Eq. 2.39
κ	mixing-length constant, [-]
ν	kinematic viscosity, $[m^2/s]$
ρ	fluid density, $[kg/m^3]$
τ_w	wall shear stress, $[kg/(m\ s^2)]$

1 Introduction

1.1 Background

Heat transfer between two fluids is an important process in many industries as it can lower the need for external cooling or heating and thus lower the operational costs of an arbitrary operation. Engineering applications where heat exchangers stands for an important part of the operation are applications which includes space heating, air-conditioning, heat recovery systems and many more [1].

A common configuration of a heat exchanger for convective heat transfer is to arrange the flow of the two fluids in a counter-current fashion, as the total energy transfer per unit area is greater in comparison to flow arranged in a co-current manner, [2]. The convective heat transfer is related to the fluid motion within the heat exchanger together with the properties of the fluid and the geometry implemented in the specific case. Unquestionably, the boundary layer, will play an important role in momentum and heat transfer which is underlined by Dipprey and Sabersky, [3]. A *thermal boundary layer* will be created due to the temperature difference between the wall and the bulk flow in the heat exchanger, which will generate inherent resistance to transfer heat from the wall to the fluid.

Improvement of heat transfer rate has been an immediate topic for a long time as low energy usage is a global goal, both in terms of economics and in relation to the environment, [4]. There is currently a great deal of effort in enhancing the heat transfer of heat exchangers where considerable research has been conducted on how to modify the interior geometry of the heat exchanger. There are several ways of modifying the geometry, such as wire coils, corrugated or dimpled tubes. The choice of a particular modification is dependent on the Reynolds number, fluid properties and particular application in comparison to enhancing heat transfer (e.g ease of cleaning). In addition to increasing the heat transfer the modification of geometry generally increases the pressure drop, due to the roughness of the individual geometry modification, [5].

In the effort to increase heat transfer performance several studies have been reported in the literature. Experiments have been done for different heat enhancement strategies at varying Reynolds numbers and roughness parameters such as different roughness heights, distance between the roughness elements and type of roughness [5–7]. Analysis of flow and thermal performance based on computational studies has been performed. Mirzaei et al. [8], used large eddy simulation (LES) to study flow and heat transfer in a channel with outward corrugated elements on one side, at different corrugation amplitudes. Lee et al. [9] and Krogstad et al. [10] used direct numerical simulations (DNS), of Reynolds number based on momentum thickness and bulk respectively of 300-1300 and 12800, to investigate how roughness affected the turbulent boundary layer and the overall flow.

This project aims at investigating how the heat transfer is enhanced using internally corrugated tubes of different designs. The goal is to develop further understanding how hydrodynamic and heat transfer resistance is affected by disturbance of the near wall region using corrugated tubes and further how this affects the heat transfer rate.

How long this enhanced heat transfer survives, and when another disturbance need to be introduced, is also investigated. The investigation is to be performed using LES. Further the structure of the corrugations will be done according to the d- and k-type pipe roughness proposed by Perry et al. [11].

2 Theroretical background

In order to fully understand how heat transfer is affected by geometrical disturbances, knowledge of how turbulence works is needed. The following section gives a theoretical background on turbulence followed by a description of LES and different subgrid models. Finally periodic boundary conditions, wall treatment and the effect of wall roughness are discussed.

2.1 Turbulence theory

Turbulence is perhaps in the eyes of an arbitrary person an unwittingly feature of everyday flows. However turbulence is a complex and important feature in many engineering flows, such as processes involving mixing, diffusion and transport of heat, mass and momentum. Thus it is of great interest to understand turbulence.

Turbulence in itself is not well defined, however it is closely connected to observation of vortices together with some distinctive features of turbulent flows which are given by Tennekes [12]. Turbulent flows are by nature chaotic with random motion of a fluid that involves several different scales of varying magnitudes, i.e. length-, time- and velocity scales. These length scales of turbulence are of larger magnitude than molecular scales and turbulence can as such be treated as a *continuum* phenomena. The largest scales are attributed to the largest of the aforementioned vortices (also called eddies), where a vortex is a reasonably coherent structure of turbulent motion over a region of space within the flow confinement. This region accommodates in addition to the larger vortices, vortices of smaller magnitudes leading to turbulent flows being *irregular*, meaning that it contains a wide range of different scales. [12, 13]

Turbulence is a *3D phenomena* due to turbulent mechanisms such as vortex stretching and vortex tilting, which are ways to describe conservation and transfer of energy of vortices of different sizes. This is closely connected to the feature that turbulent flows are *dissipative*, meaning that turbulence cannot exist without a continuous flux of energy from a source. In pipe flow the source of energy is coming from the mean flow, see section 2.1.2 for further explanation.

2.1.1 Kolmogorov's hypotheses and relation to length scales of turbulence

As stated before there are several magnitudes of scales each denoting a size of a vortex, to which there are several definitions, where some vortices are just transferring energy and other lose their energy through dissipation. In 1941 Kolmogorov stated three hypotheses, which have become a foundation for current turbulence research, [13,14]. The first hypothesis stated by Kolmogorov is in regard to isotropy of small-scale motion (i.e. small eddies). He argued that the larger eddies of scales l_0 are anisotropic (non-uniform in orientation) and that they lose directional information due to a chaotic scale-reduction process, i.e. transfers energy down to smaller eddies (because of being dissipative). The hypothesis is stated as: *At sufficiently high Re numbers, the small scales of turbulent motions ($l \ll l_0$) are statistically isotropic*, [13,14].

Kolmogorov further argued that all sense of geometry is lost as the energy from the larger eddies is passed down to smaller eddies. In that sense the statistics of the smaller and isotropic eddies could be said to be universal or similar in every high Re-number turbulent flow. It could at this point be beneficial to introduce a demarcation length scale, l_{El}, as a means of separating eddies which are isotropic and anisotropic. The processes of importance within this universal range are the transfer of energy and the viscous dissipation, which leads to Kolmogorov's second hypothesis: *In every turbulent flow at sufficiently high Reynolds number, the statistics of the small-scale motions ($l < l_{El}$) have a universal form that is uniquely determined by ν and ε*, [13,14].

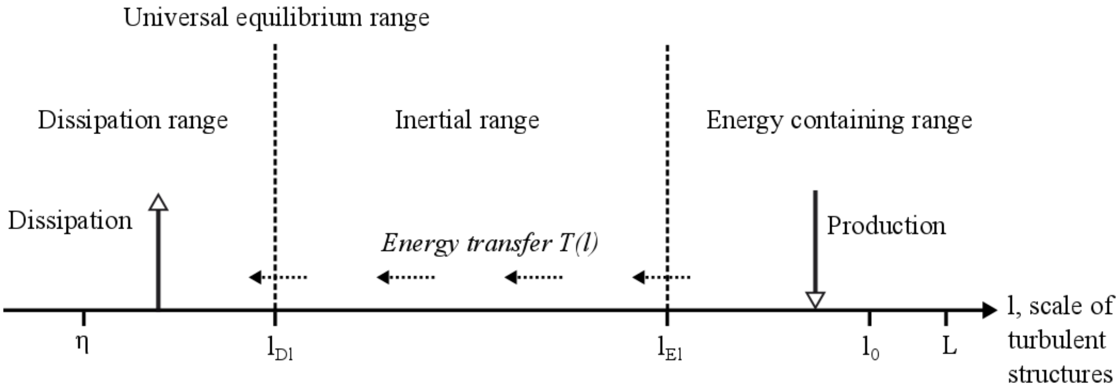

Figure 1: Energy cascade which describes the hierarchy of energy transfer in turbulent eddies, adopted from [13].

The range $l < l_{El}$, where isotropic vortices are located, is called the *universal equilibrium range*, see Figure 1, in which the eddies are of such small scale that they are assumed to be able to maintain dynamic equilibrium i.e. that production of turbulence is the same as the dissipation. The scales that describe the smallest eddies are called the Kolmogorov scales,

$$\eta \equiv (\nu^3/\varepsilon)^{1/4}, \tag{2.1}$$

$$u_\eta \equiv (\varepsilon\nu)^{1/4}, \tag{2.2}$$

$$\tau_\eta \equiv (\nu/\varepsilon)^{1/2}. \tag{2.3}$$

Here η is the Kolmogorov length scale, u_η the Kolmogorov velocity scale and τ_η is the Kolmogorov time scale. The Reynolds number based on the Kolmogorov scales is by definition 1 and as such the smallest scales are always laminar.

Kolmogorov's third hypothesis is under the assumption that there exists a range, namely called *inertial subrange*, of length scales where the viscous effect is of minor importance and such the statistics of the motion is only being dependent on the energy-dissipative rate. The approximate hypothesis is stated as follows: *In every turbulent flow at sufficiently high Reynolds number, the statistics of the motion of scale l in the range $l_0 \gg l \gg \eta$ have an universal form that is uniquely determined by ε independent of ν*, [13, 14].

Thus according to the two last hypotheses it can be concluded that the motion in the inertial subrange is solely dependent on the inertial effects of the flow while within the dissipative range the motion is dependent on the viscous effects.

2.1.2 Energy spectra

For flows of high Reynolds number there is according to the Kolmogorov hypothesis a range of different length scales. One common way of visualizing this is by plotting the so called energy spectrum. Figure 2 shows the energy spectrum which, for fully developed homogeneous turbulence, is a tool of identifying the energy distribution (see Eq. 2.4) over the different length scales. However instead of length scales the x axis is composed of the wave number κ which is inversely proportional to the radius of the eddies ($\kappa \propto 1/r$), where C_κ is a universal constant.

$$E(\kappa) = C_\kappa \varepsilon^{2/3} \kappa^{-5/3} \qquad \frac{1}{l_0} \ll \kappa \ll \frac{1}{\eta} \tag{2.4}$$

As seen in Figure 2 most of the turbulent energy is located in the larger eddies and thus has a larger impact on the turbulent transport. Equation 2.4 is also called the Kolmogorov spectrum law and states that for a flow that is fully turbulent there exists an area where the energy spectrum displays a decay in the order of -5/3, [13].

2.2 CFD simulation principles

In order to simulate physical systems, simplifications by means of introducing models that describe the behaviour of the system are needed. The fluid is assumed to follow the continuum assumption, meaning that the fluid is thought of as a continuous distribution of matter, [2, 15] as such quantities as density and pressure, among others, could vary from point to point i.e. the contribution of the molecular interaction can thus be neglected as the molecular interaction evens out sufficiently and the properties of the fluid could thus be described as continuous fields. From this, equations for conserved quantities such as mass, momentum and energy can be formulated.

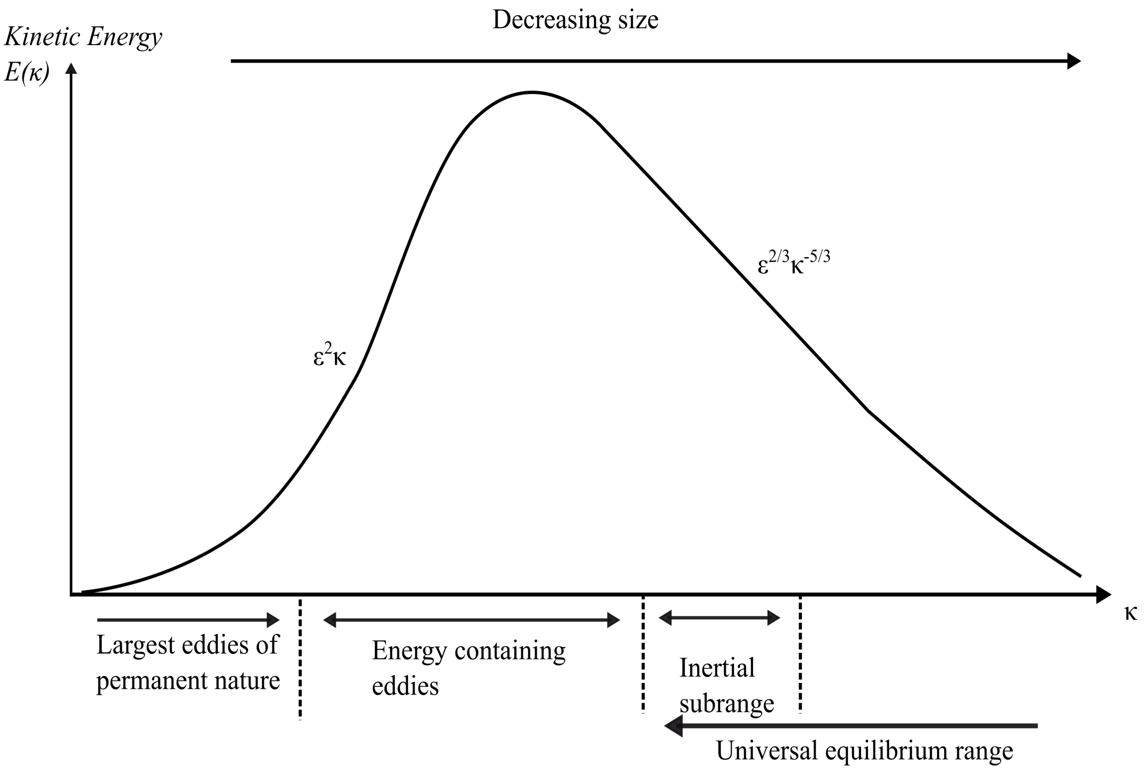

Figure 2: Energy spectrum with subranges, adopted from [13].

Conservation of mass also known as continuity, [13], describes the transport of mass within a volume and is formulated as:

$$\frac{\partial \rho}{\partial t} + \frac{\partial \rho U_i}{\partial x_i} = 0. \tag{2.5}$$

Where ρ is the density of the fluid, U_i is the flow velocity vector field and i is a dummy index of a set {1,2,3} indicating summation over the three velocity directions according to Einstein summation convention. Given the nature of waters insignificant effect on density due to pressure variations the assumption of incompressible fluid can be assumed which reduces Eq. 2.5 to

$$\frac{\partial U_i}{\partial x_i} = 0. \tag{2.6}$$

Assuming that impact due to gravity and other external forces are negligible then the conservation equation of momentum, i.e. Navier-Stokes equation, [13], becomes,

$$\frac{\partial U_i}{\partial t} + U_j \frac{\partial U_i}{\partial x_j} = -\frac{1}{\rho}\frac{\partial p}{\partial x_i} + \nu \frac{\partial^2 U_i}{\partial x_j \partial x_j}. \tag{2.7}$$

Where p is the pressure of the fluid and ν is kinematic viscosity. Note that j is here the dummy index and i is the free index.

The energy equation in its conserved form when neglecting heat addition from reactions, radiation and viscous heating (as the *Brinkman number* is lower than unity) is written as

$$\frac{\partial(\rho c_P T)}{\partial t} + \frac{\partial(\rho U_j C_p T)}{\partial x_j} = \frac{\partial}{\partial x_j}\left(\kappa \frac{\partial T}{\partial x_j}\right). \tag{2.8}$$

Where c_P is the heat capacity at constant pressure and κ is the thermal conductivity of the fluid, [13].

2.3 Large Eddy Simulations

To simulate a phenomenon of interest, a satisfactory resolution is needed to include the relevant scales present in the problem. In order to capture the true behaviour of an arbitrary phenomena it needs to be fully resolved, which can be done by doing Direct-Numerical Simulations (DNS). In DNS the turbulent flow is numerically solved directly, where no turbulence model is used. This is possible by resolving all spatial and temporal scales that is included in the phenomena. The procedure is computationally very heavy, as it would require the mesh to be very fine to resolve the scales of the bulk and near wall region, which is why DNS mainly is used as a research tool. In comparison to DNS there exists simulation tools where the conservation equations, in section 2.2, are simplified by introducing e.g. Reynolds decomposition, resulting in Reynolds Averaged Navier Stokes (RANS) turbulence models such as k-ε, k-ω and RSM. These models solve the turbulent behaviour of the flow by modelling it instead of directly resolving it by averaging over time scales larger than the largest eddies. Due to its simplicity and low computational cost RANS models have been the standard of modelling industrial applications, but as computational power increases so does the availability to move to higher resolution. A compromise between both DNS and simplified models such as the RANS models is the *large eddy simulations* (LES) which is a method of fully resolving the turbulent flow field for the larger eddies while using models to predict the behaviour of the smaller and isotropic eddies.

2.3.1 The fundamentals of LES

LES is done by implementing a spacial filtering method of the different scales found in the flow. The filtering is done to fully resolve the larger to intermediate scales while the smaller scales are modelled, [16]. The advantage of doing this is that the computational power is reduced as not all scales need to be fully resolved. Further the smaller and isotropic eddies are much easier modelled in comparison to the anisotropic larger scales, which is why models are used for the smaller scales. However one downside of LES is that one need to perform the simulations over a certain time in order to collect data that is statistically correct. This is because in LES the transient flow fields are time averaged, thus to yield proper mean fields one have to average over long enough time, which is time-consuming. Before proper data can be extracted, the flow field has to be fully developed to avoid data which is still affected by the initialization of the simulation, [13, 16].

To ensure that the LES simulation is done properly several ways of evaluating the resolution can be performed, such methods includes estimating the amount of resolved kinetic energy in relation to the total energy, i.e. $k_{resolved}/(k_{resolved} + k_{residual})$ which should always be above 80 % for a reasonable LES simulation. Two-point correlation can be performed to assess that at least 5-10 cells are resolving the largest turbulent structures. Subgrid viscosity ratio can be calculated as a measurement of the importance of unresolved scales, the smaller the ratio the better, where a value of 0 is required for DNS resolution. Finally one can check that there exist a -5/3 slope in the energy spectra that confirms the existence of the inertial subrange, [13].

2.3.2 Filtering of LES

Filtering of the turbulent scales is done by using a filter operation that spatially separates the scales of the larger and smaller eddies, a generalized filter can be defined as,

$$\overline{U_i}(x,t) = \iiint G(x-\xi;\overline{\Delta})U_i(\xi,t)d^3\xi. \tag{2.9}$$

Where the filter function (G), will act to exclude velocities (U_i) that are occurring at smaller scales than the filter width Δ and eliminating these from the solution procedure of the governing equations and instead model them using subgrid models. The velocity field will thus be decomposed into two separate fields, [13, 16],

$$U_i(x,t) = \overline{U}_i(x,t) + u_i(x,t). \tag{2.10}$$

Where $\overline{U}_i(x,t)$ is the velocity field of the resolved scales used in the filtered equations and $u_i(x,t)$ is the residual velocity flow field. Applying the filtering procedure on the Navier-Stokes- and energy equation (Eqs. 2.6-2.8) yields,

$$\frac{\partial \overline{U}_i}{\partial x_i} = 0, \tag{2.11}$$

$$\frac{\partial \overline{U}_i}{\partial t} + \frac{\partial \overline{U_i U_j}}{\partial x_j} = -\frac{1}{\rho}\frac{\partial \overline{p}}{\partial x_i} + \nu \frac{\partial^2 \overline{U}_i}{\partial x_j \partial x_j}, \tag{2.12}$$

$$\frac{\partial(\rho C_p \overline{T})}{\partial t} + \frac{\partial(\rho C_p \overline{U_j T})}{\partial x_j} = \frac{\partial}{\partial x_j}\left(\kappa \frac{\partial \overline{T}}{\partial x_j}\right). \tag{2.13}$$

Where all terms are known in terms of filtered quantities ($\overline{U}$ or $\overline{T}$) except for non-linear terms $\overline{U_i U_j}$ and $\overline{U_j T}$.

By introducing a decomposition of the two terms they can be expressed in filtered quantities and the residual stress tensor, [13], and the residual scalar flux, [17], respectively as

$$\tau_{ij}^R = \overline{U_i U_j} - \overline{U}_i \overline{U}_j, \tag{2.14}$$

$$\tau_{j,T}^{R} = \overline{U_j T} - \overline{U}_j \overline{T}. \tag{2.15}$$

Which describes the interaction of momentum and thermal energy, between different scales (including filtered and non-filtered scales), respectively and are modelled using subgrid models. The resulting filtered equations become

$$\frac{\partial \overline{U}_i}{\partial t} + \frac{\partial \overline{U}_i \overline{U}_j}{\partial x_j} = -\frac{1}{\rho}\frac{\partial \overline{p}}{\partial x_i} + \nu \frac{\partial^2 \overline{U}_i}{\partial x_j \partial x_j} - \frac{\partial \tau_{ij}^{R}}{\partial x_j}, \tag{2.16}$$

$$\frac{\partial(\rho C_p \overline{T})}{\partial t} + \frac{\partial(\rho C_p \overline{U}_j \overline{T})}{\partial x_j} = \frac{\partial}{\partial x_j}\left(\kappa \frac{\partial \overline{T}}{\partial x_j}\right) - \frac{\partial \tau_{j,T}^{R}}{\partial x_j}. \tag{2.17}$$

Now all terms are expressed in quantities that either are known or will be modelled.

2.3.3 Subgrid modelling

Subgrid models aim to model the isotropic eddies that are not being resolved by the LES procedure. Many subgrid models usually employ the concept that the momentum transport through the residual stress tensor can be modelled by a subgrid eddy viscosity which was first proposed by Smagorinsky, [18]. The concept is further developed in several other subgrid models such as the Dynamic Smagorinsky-Lily, [13], the Wall-Adapting Local Eddy-viscosity (WALE) model, [19] and the Dynamic Kinetic Energy (DKE) model, [20]. The basic idea is that the subgrid viscosity can with the help of Prandtl mixing length hypothesis enable the subgrid viscosity to be expressed by a distinctive subgrid velocity and length scale.

$$\nu_{SGS} = l_{SGS}\, U_{SGS} \tag{2.18}$$

The length scale can be assumed to be proportional to the filter size Δ times a constant C$_s$ (called the Smagorinsky coefficient), while the velocity scale is assumed to be proportional to the second invariant of the filtered strain rate tensor as $U_{SGS} = l_{SGS}|\overline{S}|$ resulting in the following

$$\nu_{SGS} = (C_s\, \Delta)^2 |\overline{S}|. \tag{2.19}$$

The Smagorinsky coefficient is needed to be known *a priori.* By modifying the filtered pressure and residual stress tensor (seen in Eq. 2.16),

$$\overline{P} = \overline{p} + \frac{1}{3}\tau_{kk}, \tag{2.20}$$

$$\tau_{ij}^{d} = \tau_{ij}^{R} - \frac{1}{3}\tau_{kk}\delta_{ij} = -2\, \nu_{SGS}\, \overline{S}_{ij}, \tag{2.21}$$

and using a linear eddy-viscosity concept, the deviatoric part of the residual stress tensor can be related to the filtered rate of strain as seen as the last part of Eq. 2.21, where $\overline{S}_{ij} = \frac{1}{2}\Big(\frac{\partial \overline{U}_i}{\partial x_j} + \frac{\partial \overline{U}_j}{\partial x_i}\Big)$.

Thus the resulting modified Navier-Stokes equation is

$$\frac{\partial \overline{U}_i}{\partial t} + \frac{\partial \overline{U}_i \overline{U}_j}{\partial x_j} = -\frac{1}{\rho}\frac{\partial \overline{P}}{\partial x_i} + (\nu + \nu_{SGS})\frac{\partial}{\partial x_j}\left(\frac{\partial \overline{U}_i}{\partial x_j} + \frac{\partial \overline{U}_j}{\partial x_i}\right). \tag{2.22}$$

Dynamic Smagorinsky-Lily model

The dynamic Smagorinsky-Lily model, [13], works by relating the subgrid scale stress at two filters of different sizes, through the introduction of a test filter, in extension to the first filter discussed in earlier sections. The test filtering denoted as "tilde" ($\sim$) is done according to,

$$\widetilde{U}_i(x,t) = \iiint G(x - \xi; \widetilde{\Delta}) U_i(\xi,t) d^3\xi. \tag{2.23}$$

Applying the test filter on the already filtered velocity field $\overline{U}_i$ then yields a double filtered velocity $\widetilde{\overline{U}}_i$, which allows for decomposition of the velocity field according to,

$$U_i = \overline{U}_i + u_i = \widetilde{\overline{U}}_i + (\overline{U} - \widetilde{\overline{U}}_i) + u_i. \tag{2.24}$$

In a similar manner as the residual stress tensor was put up a residual stress tensor for the test filter scale can be put up as,

$$T_{ij} = \widetilde{\overline{U_i U_j}} - \widetilde{\overline{U}}_i \widetilde{\overline{U}}_j. \tag{2.25}$$

By applying the test filter on Eq. 2.14 the residual stress tensor becomes,

$$\widetilde{\tau}_{ij} = \widetilde{\overline{U_i U_j}} - \widetilde{\overline{U}_i \overline{U}_j}. \tag{2.26}$$

Subtracting this equation from Eq. 2.25 then one get the resolved turbulent stress tensor (also known as the Germano identity),

$$L_{ij} = T_{ij} - \widetilde{\tau}_{ij} = \widetilde{\overline{U_i U_j}} - \widetilde{\overline{U}}_i \widetilde{\overline{U}}_j - \left(\widetilde{\overline{U_i U_j}} - \widetilde{\overline{U}_i \overline{U}_j}\right) = \widetilde{\overline{U}_i \overline{U}_j} - \widetilde{\overline{U}}_i \widetilde{\overline{U}}_j. \tag{2.27}$$

By then taking the deviatoric part of the stress tensor and the test stress tensor and defining

$$M_{ij} = 2\overline{\Delta}^2 \widetilde{\overline{S}\,\overline{S}_{ij}} - 2\widetilde{\overline{\Delta}}^2 \widetilde{\overline{S}}\,\widetilde{\overline{S}}_{ij}, \tag{2.28}$$

yields the Dynamic Smagorinsky constant c_s in terms of the deviatoric stress tensor L_{ij}

$$L^d_{ij} = L_{ij} - L_{kk}\delta_{ij} = T^d_{ij} - \widetilde{\tau}^d_{ij} = c_s M_{ij}. \tag{2.29}$$

However c_s is in tensorial form and thus a least square minimization method is used to yield one equation. Furthermore the constant is averaged in space or time (possibly both) to enable the constant to sustain numerical stability during the simulation yielding the final equation for the dynamic Smagorinsky constant,

$$c_s = \frac{\langle M_{ij} L_{ij} \rangle}{\langle M_{kl} M_{kl} \rangle}, \tag{2.30}$$

which is used instead of the Smagorinsky coefficient in Eq. 2.19.

WALE model

The WALE model was first introduced by Nicoud and Ducros, [19], who used the deviatoric part of the square of the velocity gradient to estimate the eddy-viscosity,

$$S^d_{ij} = \frac{1}{2}(\overline{g}^2_{ij}\overline{g}^2_{ji}) - \frac{1}{3}\delta_{ij}\overline{g}^2_{kk}, \quad \text{where } \overline{g}_{ij} = \frac{\partial \overline{U}_i}{\partial x_j}. \tag{2.31}$$

The eddy-viscosity is then expressed as spatial operators together with scaling to account for the correct behaviour close to the wall according

$$\nu_{SGS} = (L_s)^2 \, \frac{(S^d_{ij} S^d_{ij})^{3/2}}{(\overline{S}_{ij}\overline{S}_{ij})^{5/2} + (S^d_{ij} S^d_{ij})^{5/4}}, \tag{2.32}$$

where $L_s = C_w \, \Delta$ which is similar to length scale stated for the Smagorinksy model where it in this case is a WALE coefficient, [19].

DKE model

The DKE model proposed by Kim and Menon, [20], uses the subgrid kinetic energy to yield a dynamic expression for the eddy-viscosity and thus uses a similar test-filter mentioned for the Dynamic Smagorinsky-Lily-model.

The velocity scale is then characterized using the subgrid kinetic energy

$$U_{SGS} = k^{1/2}_{SGS} = \Big(\frac{1}{2}(\overline{U_k U_k} - \overline{U}_k \overline{U}_k)\Big)^{1/2}, \tag{2.33}$$

where k_{SGS} is the subgrid kinetic energy. Note that the usage of the kinetic energy results in one additional transport Eq. for k_{SGS} to solve.

The length scale is characterized by $\overline{\Delta}$ which is the test-filter size times a dynamically determined coefficient C$_\tau$ yielding the eddy-viscosity as

$$\nu_{SGS} = C_\tau \, \overline{\Delta} k_{SGS}^{1/2}. \tag{2.34}$$

2.4 k-ω SST

The k-ω SST model is a RANS model that integrates through the boundary layer down to y^+ close to 1 as it uses the k-ω model in the wall region and k-ε in the bulk. It is allegedly better at predicting the boundary layer behaviour with adverse pressure gradients, due to modification of the turbulent viscosity definition, introduction of blending functions and incorporation of a damped cross-diffusion derivative term in the ω equation, [13, 21, 22].

2.5 Boundary conditions

For internal flow within a tube the evolution of the boundary layer will be dependent on the development of a fully developed velocity profile. This means that the viscous effect that occurs due to the shearing of fluid-fluid and wall-fluid interaction has to stabilize, with respect to the streamwise direction in order to be able to acquire statistical stable flow properties. Experimentally one can perform measurements an arbitrary distance away from the inlet of the pipe, where the velocity profile yet has to develop, in order to reach a fully developed velocity profile. In simulations however there are several means of achieving a fully developed velocity profile, an extension of the geometry can be made where the flow is enabled to stabilize before reaching the point of interest. One can after having run a simulation for a while, copy flow properties from a plane close to the exit of the computational domain and use as inlet boundary conditions, which is repeated until a fully developed profile is achieved i.e. when $\dfrac{\partial U_i}{\partial x_i} = 0$ at the boundary, [23]. Yet another method can be utilised, which is the use of periodic boundary conditions (PBC). The PBC method allow to perform flow simulations where the velocity profile is fully developed, through an iterative manner, while limiting the computational power by using smaller sections of the geometry.

This is done under the assumption that the velocity within the geometry is periodic [22] i.e.,

$$U_i(\widehat{r}) = U_i(\widehat{r} + \widehat{L}) = U_i(\widehat{r} + 2\widehat{L}) = ... \tag{2.35}$$

Where $\widehat{r}$ is the position vector (x,y,z) within the geometry and $\widehat{L}$ is the periodic length vector, in this case only containing the streamwise component (z-direction). This then replaces the criteria of $\dfrac{\partial U_i}{\partial x_i} = 0$ as a boundary condition with [24],

$$U_i(x,y,0) = U_i(x,y,L). \tag{2.36}$$

Where the computational domain will mainly be limited by the choice of L (and x,y but they are in this case limited by the diameter of the pipe), which can be arranged to pseudo-optimize the computational requirements of the simulation. In order to establish periodic boundary conditions for perpetual flow a correction to the pressure calculation need to be done to prevent inherent build-up of pressure drop as the iterations proceeds. The pressure in itself is not periodic as the case of velocity; however the pressure drop is periodic and can be expressed as,

$$\Delta p = p(\widehat{r}) - p(\widehat{r} + \widehat{L}) = p(\widehat{r} + \widehat{L}) - p(\widehat{r} + 2\widehat{L}) = ... \tag{2.37}$$

For this study, where the flow is incompressible, the treatment of the pressure in terms of periodicity is to decompose the pressure into two parts, according to,

$$\frac{\partial p}{\partial x_i} = \beta \frac{\widehat{L}}{|\widehat{L}|} + \frac{\partial p'}{\partial x_i}. \tag{2.38}$$

Where p' is the periodic pressure and β is the linearly-varying component of the pressure.

In addition to modifying the pressure, the temperature need to be modified as well to account for streamwise periodic boundary conditions. For the case of constant wall temperature, a scalar function, which conforms with the periodic conditions over the domain limited by L, is introduced,

$$\theta = \frac{T(\widehat{r}) - T_w}{T_{bulk,inlet} - T_w}. \tag{2.39}$$

Where $T(\widehat{r})$ is the temperature of position vector $\widehat{r}$, T_w is the wall temperature and $T_{bulk,inlet}$ is the bulk temperature defined as $T_{bulk,inlet} = \frac{\int_A T|\rho \mathbf{v} d\mathbf{A}|}{\int_A |\rho \mathbf{v} d\mathbf{A}|}$ where A is the inlet cross-sectional area of the pipe. The scalar function will enable the temperature to behave in a periodic behaviour and thus avoid excess build-up of enthalpy.

2.6 Wall treatment and turbulent boundary layers

The near-wall region is an area which is of high importance when performing simulations. It can affect the reliability of the numerical solution, as the wall is the main source of vorticity and turbulence, [22]. In the near-wall region high gradients of variables such as velocity but also of scalars such as temperature are present, which makes the treatment of the near-wall region an important part to a successful simulation.

At a solid wall the relative velocity between the wall and adjacent fluid is zero. This is called the no-slip condition and is the reason for the creation of a boundary layer close to the wall. Prior to the collision with the wall the molecules move with a velocity of the mean field with an addition of the random molecular motion of fluid particles. As the fluid molecules collide with the wall the relative velocity (momentum) becomes zero and the molecule linger for a brief moment until they leave the surface in a random direction. The combined effect of these molecules which has "bounced" away from the wall, results in slowing the adjacent molecules further away from the wall and as such forming a *boundary layer*, [13, 25]. Within this boundary layer the velocity of the fluid slowly decreases from the mean flow, in the bulk, to zero at the wall. In a similar way there exists a thermal boundary layer, which is caused by the finite temperature specified at the wall being different from the bulk temperature.

The behaviour of a boundary layer present at the wall varies and can either be laminar or turbulent dependent on the Reynolds number. The difference being that the turbulent boundary layer is characterized by unsteady swirling of of the flow which yields higher mass, heat and momentum transfer, in comparison to the laminar case. However as the momentum transfer is increased, so does the wall shear stress and thus increases the pressure drop required to overcome for a flow of a fixed quantity, [13]. This is caused by turbulent mixing which dissipates a lot of energy and thus causes an increase in resistance for the flow to pass, [25].

Flow within an arbitrary geometry can be divided into two regions; one outer region where the effect of the wall is negligible, and one inner region where the effect has to be taken into account.Turbulent boundary layers are, shown from experiments, often divided into sub-layers, [22]. The sub-layer furthest from the wall, also referred to as *fully turbulent sub-layer*, is predominately turbulent and thus dependent on the turbulent stresses as the viscous effect of the wall is negligible at that point. The other two layers however, namely the *viscous sub-layer* and the *buffer sub-layer* cannot neglect the viscous effect. In the viscous sub-layer the flow is close to being laminar as the viscous effects (stress) is high and as the name implies, is the prominent cause of momentum transport in this sub-layer. The third and last sub-layer is the buffer layer which is an area of transition between the viscous and fully turbulent sub-layers where both the viscous and turbulent stresses are of equivalent importance. Common practice is to express the distance, from the wall, of these sub-layers in terms of variables of the wall.

The characteristic velocity scale of the turbulent, fluctuating motion of the sub-layer scale u_τ, often referred to as the friction velocity, can be expressed by assuming constant wall stress, [25],

$$u_\tau = \sqrt{\frac{|\tau_w|}{\rho}}. \tag{2.40}$$

Where τ_w is the wall shear stress defined by $\tau_w = -\rho\overline{u'v'} + \rho\nu\dfrac{d\overline{u}}{dy}$. By defining a length scale based on the friction velocity, $l_\tau = \nu/u_\tau$, where ν is the kinematic viscosity, yields a Reynolds number of 1 and thus relating the velocity- and length scale to the laminar region close the wall.

By scaling the velocity and the physical distance from the wall with friction variables we obtain in dimensionless form

$$U^+ = \frac{U}{u_\tau}, \tag{2.41}$$

$$y^+ = \frac{y u_\tau}{\nu}. \tag{2.42}$$

Based on the dimensionless wall distance (y^+) the three sub-layers can, after measurements performed by H. Reichardt, [25], close to the wall, be expressed as follows:

Viscous sub-layer:	$0 < y^+ < 5$
Buffer sub-layer:	$5 < y^+ < 30$
Fully turbulent sub-layer:	$y^+ > 30$

Typically these sub-layers can be identified for an arbitrary experiment or simulation by simplifying the total stress tensor. The total stress tensor is written as follows,

$$\tau_{xy} = \rho\nu \frac{d\langle U_x \rangle}{dy} - \rho\langle u_x u_y \rangle, \tag{2.43}$$

where the first term on the right-hand side (RHS) is the viscous stress and the other RHS term is the Reynold stress (inertial stresses), [13].

By assuming that the total stress close to the wall is only due to viscous stress and is constant the stress tensor can be rearranged and integrated with respect to the wall distance y to yield, [13],

$$\langle U_x \rangle = \frac{\tau_w y}{\rho\nu} = \frac{u_\tau^2 y}{\nu}. \tag{2.44}$$

Refering back to Eqs. 2.41 and 2.42 this can be expressed in dimesionless form as

$$\langle U_x \rangle^+ = y^+. \tag{2.45}$$

By doing a similar assumption of the total stress but in the fully turbulent sub-layer the total shear stress can be expressed as only to be affected by the Reynolds stress (inertial component),

$$\tau_w = -\rho\langle u_x u_y \rangle. \tag{2.46}$$

By using Prandtl's mixing length hypothesis, [25], and introducing a Prandtl's mixing length as $l = \kappa y$, where κ is an experimental constant later referred to as the von Kármán constant (∼0.42), the above equation can be rewritten as

$$\frac{\tau_w}{\rho} = -\rho\langle u_x u_y \rangle = l^2 \left(\frac{d\langle U_x \rangle}{dy} \right)^2 = \kappa^2 y^2 \left(\frac{d\langle U_x \rangle}{dy} \right)^2. \tag{2.47}$$

Further simplification can be done knowing the friction velocity (Eq. 2.40). By then integrating the resulting equation one obtains the logarithmic velocity profile which in dimensionless terms is expressed as

$$\langle U_x\rangle^+ = \frac{1}{\kappa}\, ln(y^+) + B, \tag{2.48}$$

where B is an intersection constant found through experiments to be around 5.

Similar logarithmic profiles can be developed for other quantities than velocity such as the temperature. For the near wall area the temperature is supposed to vary with the Prandtl number and the dimensionless wall number, [26],

$$\langle T\rangle^+ = Pr\; y^+. \tag{2.49}$$

For the inertial range the temperature will vary as, [13, 25, 27],

$$\langle T\rangle^+ = \frac{1}{\kappa_T}\, ln(y^+) + B_T, \tag{2.50}$$

where κ_T and B_T are dependent on the Prandtl number accordingly, $\kappa_T = \kappa/Pr_t$ and $B_T = 13.7\; Pr^{2/3} - 7.5$, where Pr_t s the turbulent Prandtl number, [13,25].

The temperature is scaled as follows,

$$\langle T\rangle^+ = \frac{(T_w - T)\; \rho\; c_P\; u_\tau}{q}, \tag{2.51}$$

where q is the heat flux through the wall.

2.6.1 Surface roughness

Until this point the walls of the geometry has always been assumed to be *hydraulically smooth* in nature. By introducing wall roughness into a flow the overall momentum, heat and mass transport is increased, as a result of the roughness disturbing the hydrodynamic and thermal boundary layers, [13]. However the effect of this is limited to roughness height (k) larger than the thickness of the viscous sublayer, [13, 25, 28]. The roughness can be expressed in dimensionless form as,

$$k^+ = \frac{k u_\tau}{\nu}. \tag{2.52}$$

It has been shown through experiments by Tani [29], and mentioned by Schlichting and Gersteg, [25] and Cebeci and Bradshaw, [28], that the velocity profile for flow with rough surfaces exhibit a similar logarithmic behaviour as seen for the smooth case (Eq. 2.48). The difference being that an additive constant ΔB is present in the rough case,

$$\langle U^+ \rangle = \frac{1}{\kappa} \, ln(y^+) + \Delta B(k^+), \tag{2.53}$$

which is dependent on the dimensionless roughness height and the type of roughness (e.g uniform sand, corrugations, ribs etc) used,

$$\Delta B(k^+) = C - \frac{1}{\kappa} \, ln(k^+). \tag{2.54}$$

Here C is a constant of integration which is equal to 5 (same as B in Eq. 2.48) for smooth tubes and different when roughness is important. As such it would be expected that from an arbitrary roughness there would be a parallel downward shift of the logarithmic curve. It has further been seen that there exists three distinct regimes depending on the value of the dimensionless roughness height [25][1]:

Hydraulically smooth: $0 < k^+ < 5$
Transition region: $5 < k^+ < 70$
Fully rough: $k^+ > 70$

where the fully rough region is when the roughness height is much larger than the viscous sublayer and thus fully disturbs and as such decoupled from the dependency of the molecular viscosity. In comparison the hydraulically smooth region represent the opposite where the roughness height is smaller than the viscous sublayer and as such do not yield any noticeable effect on the parallel shift and thus result in a behaviour displayed by Eq. 2.48.

In the case of fully rough regime the additive term C is 8.0 according to Schlichting, [25], and 8.5 according to Cebeci and Bradshaw, [28].

The temperature wall function for roughness elements of sand-grain roughness is proposed by Kays and Crawford, [26] to have the form of:

$$T^+ = \frac{1}{St_k} + \frac{Pr_t}{\kappa} \, ln\Big(\frac{32.6 \, y^+}{k^+}\Big), \tag{2.55}$$

where St_k is a constant which is determined experimentally. Dipprey and Sabersky, [3] correlated data to form the following equation,

$$St_k = C_s (k^+)^{-0.2} \, Pr^{-0.44}, \tag{2.56}$$

where C_s is constant given the value of 0.8 for closely packed spheres [30].

3 Methodology

In the beginning of this chapter the geometry and meshing is described. The numerical method together with the empirical correlations used in this study is then

---

[1] Note that these limits are varying depending on source as Cebeci and Bradshaw [28], indicate different values for the regimes and the additive constant compared to Schlichting [25]

presented. The geometry and corresponding mesh was generated in ANSYS Workbench v.17.

3.1 Geometry and meshing

The smooth tube used as a reference is generated by making a pipe of 5 cm in diameter and further extruding it to desired length, see Table 1 and Figure A.1a in Appendix A.

The mesh was created by performing a sweep method where an arbitrary sweep element size was chosen to be able to control the stretching of the cells in the streamwise direction. Inflation layers were added to either accommodate the RANS simulations prior to the switch to the LES model, [13]. First layer heights was estimated based on goal $y^+ \leq 1$ and estimation of wall shear stress (τ_w). The mesh was structured by hexagonal elements where the number of inflation layers was varied to ensure good transition between the cells, close to the wall, and the cells in the bulk.

Table 1: The streamwise dimension of the different tubes and the corresponding mesh size

Geometry	**Length [cm]**	**Spacing p [cm]**	**p/e**	**Cells [million]**
Smooth	20	-	-	0.34, 4.0, 17
p/e = 2.2	6.1	0.55	2.2	8.7
p/e = 10	2.5	2.5	10	4.0
p/e = 20	5.0	5.0	20	6.5

The disturbance within the tube was introduced by creating sections of internal corrugations, see Figure A.1, in Appendix A, where the roughness height is set to 0.25 cm. The geometries of the corrugations simulated can be seen in Table 1. With the pattern function the corrugation could then be placed a specific space or pitch (p) apart until desired d-, intermediate or k-type corrugation was established, see Table 1.

The mesh procedure for the rough cases was generated differently than the smooth case. Instead of having a single body to mesh, the geometry was divided into a center cylinder for the bulk and two separate volumes for the near region, see Figures A.1b-A.1d. The two outer volumes was meshed around the streamwise axis[2], which yielded satisfactory mesh properties of maximum aspect ratio and skewness below 20 (at the walls) and 0.95 respectively [13]. The mesh resolution was, for the rough tubes, managed by keeping a constant ratio of number of mesh elements to streamwise length (N/z). The ratio that was used was around 1.4[3].

---

[2] It was tried to perform the same procedure as the smooth case but that yielded a mesh with very thin slices of too high aspect ratio, close to the corrugation.

[3] This was mainly to limit the number of mesh elements.

3.2 Numerical method

The simulations were done using Fluent v.17 which is a finite volume solver where the dynamic Smagorinsky-Lily subgrid model will be employed, as it in relation to the standard Smagorinsky model does not need any *a priori* determination of the Smagorinsky coefficient C_s, but instead allows calculation of the coefficient during the simulation. Furthermore the simulation for the smooth tube was investigated by testing two additional subgrid models, namely the WALE- and dynamic kinetic energy (DKE) model.

3.2.1 Boundary conditions

At the solid wall of the pipe, no-slip boundary condition is applied. Further, in the heat transfer simulations the fluid inside the pipe will be heated up and thus the thermal boundary conditions used is that of constant wall temperature at 60 °C and an inlet bulk temperature of 20 °C. The Prandtl number is kept constant in the simulations at 6.9.

Periodic boundary conditions are used, as described in section 2.5, where the pressure drop is solved by iterative calculations of β and the temperature is scaled using Eq. 2.38 and 2.39 respectively. The periodic boundary condition is chosen to be calculated from a fixed mass flow of 0.787 kg/s based on geometry and chosen Reynolds number of 20000 of the smooth case.

3.3 Flow, turbulence and heat transfer analysis

The analysis procedure consists of two parts, one of which each tube design is run with the k-ω-SST model. This is to be compared both to empirical correlations, see section 3.3.3, and later on LES simulations.

3.3.1 k-ω SST

The k-ω SST model, was solved together with the SIMPLEC algorithm for the pressure-velocity coupling. It iterates the pressure until the continuity equation is satisfied, similar as SIMPLE, with the exception that the SIMPLEC solver is formulated to accelerate the convergence, if the issue lies in the pressure-velocity coupling. This is a result of a difference in the cell face flux expression. A production limiter is included in the SST model in order to dampen the production of turbulent energy in areas of stagnation. To account for the variation in the streamwise curvature in the roughness cases a curvature correction term is introduced to sensitize the turbulent production term to account for sudden curvature change, [22]. The spacial discretization is first order upwind schemes in order to stabilize the numerical procedure, together with second order for pressure and least squares cell based method for gradient. The under relaxation factors (URF:s) for pressure and energy are 0.9 and 0.7 respectively, which is based on the usage of SIMPLEC, and necessity to get a stable solution.

For each k-ω SST simulation a standard initialization is done according Appendix B.

3.3.2 Large eddy simulation and data analysis

The LES simulation was done by using k-ω SST simulation results as starting values, on the mesh that is used for the desired LES. Synthetic turbulence was superimposed on the mean field when the k-ω SST model was converged. Sampling was started when relatively stable monitors of wall heat-flux, wall shear stress, and periodic statistics of pressure gradient and temperature ratio was observed.

The subgrid turbulence model chosen was the dynamic Smagorinsky-Lily, as it does not need any input for the Smagorinsky coefficient but would be solved dynamically during the simulation and no extra equations to be solved (as in the case of DKE), see section 2.3.3.

SIMPLEC was used for the pressure-velocity coupling and the spatial discretization were least squares cell based method for gradients, second order schemes for pressure and energy, and bounded central differencing scheme for momentum, in order to meet requirement for conservativeness, boundedness and transportiveness. Time discretization is done with a second order implicit scheme, where the time-step is calculated from the convective time-scale. The time-step and the URF:s are chosen in order to reduce the number of internal iterations to a maximum of 20.

Sampling of the time-averaged quantities was done for an arbitrary amount of residence times, dependent on the length of the computational domain, until statistically steady values was obtained. The data is averaged in the radial and streamwise direction, however for the simulations of corrugations (p/e = 10 and 20) this is not done. This was compensated for by sampling for a longer time to yield satisfactory statistics. The data will further be constrained by introducing a virtual origin of the rough wall as proposed by Cui, Patel and Lin, [31]. Data will thus be taken from this virtual origin and to the center of the pipe. The virtual origin will be determined at a point where the streamwise velocity is zero.

3.3.3 Validation of simulations

One way to verify that the simulation results matches reality is to compare with empirical correlations. The hydrodynamics of the flow was analyzed using correlations from preceding work of von Kármán and Nikuradse, [2, 32], displayed for smooth and roughness by Eqs. C.1 and C.2 in Appendix C.

Thermal performance will be analyzed using correlations from Dittus and Boelter, [2] and Bhatti and Shah, [33], Eqs. C.3 and C.4.

Note that the formulas for roughness are formulated to suite Nikuradse-like roughness and as such not applicable in cases where the roughness elements are separated of an arbitrary distance. In that case the results will be mainly compared to the correlations below which only handles the hydrodynamics of the case.

The first correlation that takes the distance between the correlation into account is the one from Webb, Goldstein and Eckert, [7], which investigated square formed ribs at p/e ratios of 10-40, Eq. C.5.

The second one which will be used is the one from Ravigurarajan and Bergels, [34] who summaries data from several tube configurations, Eq. C.6.

In addition to the use of correlations the LES will be scrutinized regarding the ratio of resolved energy and the subgrid viscosity ratio see section 2.3.1. Further the presence of an inertial subrange is also a method used to validate LES simulations, however this was not made in this study but the reader is referred to the study performed by Ghasempour [35], where an inertial subrange is identified for the case of a smooth tube with the same geometry and flow characteristics.

4 Results and discussion

In this section the results from the mesh resolution study and comparative study of different subgrid models are presented together with hydrodynamic and thermal performance, which are compared to correlation from section 3.3.3. Finally dimensionless velocity and temperature profiles are presented and discussed, for different tube designs.

4.1 Analysis of smooth tube

Table 2 summarizes the pressure drop, amount of resolved energy and viscosity ratio for the LES simulations of the smooth tube using different mesh resolutions, where the dynamic Smagorinsky-Lily subgrid model was employed. The mesh resolution study showed discrepancies in terms of the pressure drop estimation. The low mesh resolution yielded a too low pressure drop whilst the high mesh resolution uses excessive computer power as a mesh of 4 M cells is sufficient enough to yield a good LES resolution. In total the pressure drop of the intermediate and fine mesh vary within less than 2 %. The pressure drop calculated from a common correlation (Eq. C.1) was estimated to 41.73 Pa/m. Thus even the fine mesh yields a too low pressure drop but within acceptable boundaries as it differs by 4.6 %, or 6.3 % for the intermediate mesh resolution.

The resolved energy is above 80 % for all three mesh sizes and the viscosity ratio decreases as the resolution is refined, and is thus of good LES resolution. The pressure drop is reasonably predicted using a resolution 4 M without using too much computer power and thus chosen as reference for the simulations of rough wall geometries.

Table 2: Pressure drop, resolved energy and viscosity ratio from LES simulations.

	ΔP_{drop} [Pa/m]	**Resolved energy ratio**	**Viscosity ratio**
0.34 M	32.71	0.85	0.38
4 M	39.10	0.93	0.11
17 M	39.81	0.95	0.07

Velocity profiles based on the dimensionless parameters are shown in Figure 3, where the LES data is compared to DNS data from Khoury et al. [36]. In the wall near area all simulations collapse on $U^+ = y^+$. In the outer region the graphs of the intermediate and the fine mesh are closely following each other and depict a similar pattern as the DNS data from Khoury et al. [36] for Re = 19000. The DNS and LES data does not collapse onto the wall function (Eq. 2.48). Research done by Khoury et al. [36] and Eggels et al. [37], who both performed DNS simulation of turbulent pipe flows for relatively low Reynolds numbers (down to 5300 for Khoury et al. and 7000 for Eggels et al.), show a similar shift from the "general" wall function for smooth walls. From their respective studies the validity of the smooth wall function was questionable for turbulent flows at low Reynolds number, as their data did not collapse on the wall function, but instead was shifted above it. This was further confirmed by HWA, LDA and PIV measurements by Eggels et al. [37]. The LES data obtained in this project seem to indicate the same trend as data from Khoury et al., however the LES data is shifted upwards in relation to the DNS data. This is believed to be due to the difference in flow characteristics (Reynolds number) but also as previously mentioned that the pressure drop is slightly under predicted in comparison to correlations, shown in Table 5.

The low mesh resolution however does not follow either the DNS or the other LES data, as it is shifted above. This is believed to be a result of how the normalization of the dimensionless velocity is done (Eq. 2.41). As the pressure is underestimated the resulting friction velocity will also be underestimated, thus resulting in a positive displacement of the curve.

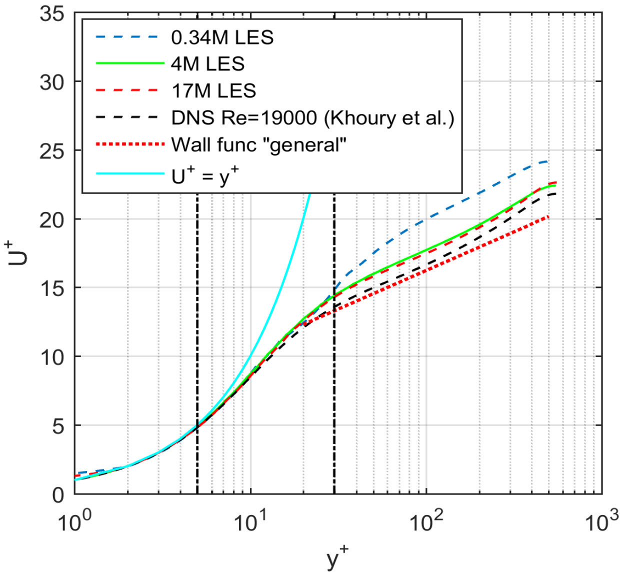

Figure 3: Dimensionless velocity profile, compared with DNS data of Re = 19000 from Khoury et al. [36].

Table 3 shows the resulting pressure drop and Nusselt number for each subgrid model. The pressure drop and Nusselt number varies by 0.1-0.5 % between the different models. The Nusselt number from a common correlation (Eq. C.3) was estimated to 138.15. The estimated pressure drop and Nusselt number are within 5.8-7.2 and 0.9-2.3 % compared to correlations for smooth tube.

Table 3: Pressure drop and Nusselt number for LES simulations of smooth tube with different subgrid models for a mesh resolution of 4 M.

	ΔP_{drop} [Pa/m]	**Nusselt number [-]**
Dynamic Smagorinsky-Lily	39.10	140.77
WALE	39.29	139.39
Dynamic Kinetic Energy	38.74	141.39

The similarities is further emphasized in Figure 4 where the LES simulations with varied subgrid models are visualized in the form of dimensionless parameters. It can be pointed out that the difference between the subgrid models is small, as they collapse on each other in the wall near area and good agreement in the outer region.

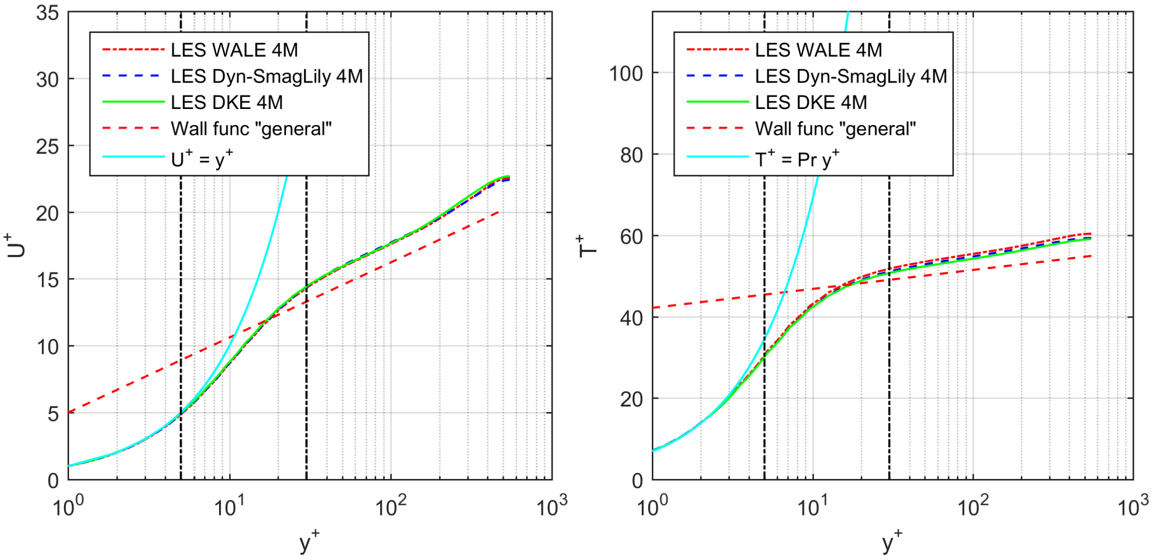

(a) Velocity profile **(b)** Temperature profile

Figure 4: Simulations performed on the smooth case with varied subgrid at 4 M mesh resolution, compared with the "general" wall function, Eq. 2.48 and Eq. 2.50.

The variation of the subgrid model indicated small dependence on the subgrid model as all models yielded similar results in both pressure drop and Nusselt number. However the small difference in the outer region indicate that the usage of the dynamic Smagorinsky-Lily subgrid model yields the least shifted data set in comparison to the DNS data by Khoury et al. [36]. As this is only done for the smooth tube, any discussion regarding the choice of subgrid model, is not done for the remaining simulations of different rough wall geometries, where the dynamic Smagorinsky-Lily subgrid model is used.

4.2 Analysis of corrugated tubes

Table 4 shows the resolved energy and viscosity ratios for the simulation of smooth and the rough tube designs. It can be concluded that the resolution of the LES is of good quality as all the simulations are resolving more than 90 % of the kinetic energy and have low viscosity ratios, [14].

Table 4: The amount of mean resolved energy, viscosity ratio for the different simulations.

	Resolved energy	**Viscosity ratio**
Smooth LES	0.93	0.11
p/e = 2.2 LES	0.94	0.10
p/e = 10 LES	0.95	0.18
p/e = 20 LES	0.95	0.14

The hydrodynamic and thermal performance parameters for the LES simulations together with empirical correlations and results from RANS simulations are summarized Table 5 and 6.

Table 5: Pressure drop for each tube, where the pressure drop is given in [Pa/m] (streamwise direction).

	ΔP_{CORR}	ΔP_{RANS}	ΔP_{LES}
Smooth	41.73[4]	42.67	39.10
p/e = 2.2	116.22[5]	139.96	134.31
p/e = 10	471.49[6] / 228.25[7]	177.46	297.78
p/e = 20	290.73[8]	162.51	232.47

The LES for the densely packed corrugations (p/e = 2.2) showed that the pressure yielded a reasonable agreement with its correlation. The correlations used for the case of p/e = 2.2 were those of Nikuradse sand roughness of the same roughness height as in this study. This can be expected to yield a lower pressure drop compared to this study as the flow is more hindered (p/e = 2.2) as the corrugations consists of half-cylinders and not spheres. Furthermore Table 5 shows that the pressure drop for both p/e = 10 and 20 is in fair agreement with their respective correlations. However a few numbers of correlations exist for when the roughness elements are introduced and the distance between them increased. For the cases of p/e = 10 and 20 the correlation of Webb, Goldstein and Eckert, [7] (Eq. C.5), relies on data of square corrugations and not rounded corrugations which would yield a higher pressure drop due to the square ribs blocking more of the flow. However another correlation from Ravigururajan and Bergels, [34] (Eq. C.6) was found that included data from rounded corrugations which yield a lower pressure drop than the correlation from Webb et al. Though caution should be taken regarding the validity of these correlations, as the data of Ravigururajan and Bergels is for maximum p/e ratio of 7 and thus would be questionable even though a relatively good match with the LES data is achieved.

The thermal performance of the smooth and densely packed roughness were of good agreement between correlations and LES simulations, where both LES simulations differed by 1.6 and 1.3 % from their respective correlation (Eq. C.3 and C.4). In general it can be shown in Table 6 that the overall thermal performance is increased as the roughness elements are introduced, and further enhanced as the distance between the corrugations is increased until a certain point, close to p/e = 10, where a maximum of 218 % increase in heat transfer is achieved in comparison to the smooth tube. However a similar trend can be seen with the pressure drop which was increased for all designs but had a maximum for p/e = 10 where it was increased by 662 %, shown in Table 5. This is expectd as the corrugations introduce hindrance of the flow and as such increases the pressure drop which is an unavoidable result of increasing the thermal performance by introduction of roughness elements. However as shown in Tables 5 and 6 is that the p/e = 2.2 yields a considerably lower pressure drop in relation to its enhancement in heat transfer performance compared to the other design. As the heat transfer performance is increased by around 200 % for

---

[4] Appendix C, Eq. C.1 [2].

[5] Appendix C, Eq. C.2 [2].

[6] Appendix C, Eq. C.5 [7].

[7] Appendix C, Eq. C.6 [34].

[8] Appendix C, Eq. C.5 [7].

all the designs, a trade-off of achieving higher thermal performance in relation to the allowable pressure drop has to be done. Furthermore the maximum of the pressure drop and thermal performance close to p/e = 10 is in agreement with simulations performed by Okamoto et al. [38], who investigated square ribs using LES, for different pitch to roughness height ratios.

Table 6: Overall Nusselt number for each tube.

	Nu_{CORR}	Nu_{RANS}	Nu_{LES}
Smooth	138.15[9]	162.25	140.77
p/e = 2.2	420.00[10]	384.97	425.36
p/e = 10	-	254.85	448.01
p/e = 20	-	269.22	390.85

The RANS simulation is shown to yield similar pressure drop and thermal performance for the cases of smooth and p/e = 2.2 as the LES and correlations, but poor agreement for the cases p/e = 10 and 20. In the RANS modeling the quantities are averaged over scales larger than the largest eddies and thus do not take the impact of the different scales into account. As such it would make sense that the RANS models yields poor agreement as the corrugations are introducing disturbances of the boundary layers and inertia to the flow, which includes several different scales. Furthermore the RANS is done in steady-state and thus the dynamic behaviour of these scales at the recirculation zones is not captured, in comparison to the LES. The dynamic behaviour, in terms of dynamic reattachment and recirculation, is further increased as the distance between the corrugation is increased. The dynamic behaviour of these scales is not included in the RANS simulations resulting in underestimated pressure drop and Nusselt number as the dynamic behaviour affects the disruption of the boundary layers at the wall. The good agreement of the smooth and p/e = 2.2 case is believed to be a result of the dynamic behavior not being a big part of the flow as in the smooth case there is no recirculation. However, p/e = 2.2 does include densely spaced corrugations which enables steady recirculation zones that do not add any dynamic behaviour to the overall flow and thus yielding a good agreement with the LES simulations and the correlations.

4.3 Analysis of boundary layers

The velocity profiles for the simulations with rough tube design are depicted in Figure 5. The vectors are fixed to have the same length but the magnitudes of cases p/e = 10 and 20 are multiplied by 2 respective 4 in order to enhance visualisation. It can be seen for the case of p/e = 2.2, the boundary layer is fully disturbed as the small space between the corrugations invoke the formation of stable recirculation zones, resulting in the boundary layer at the wall being decreased in thickness. The recirculation can be seen by noting the change in velocity direction. It is further noted that the flow close to the wall, between the corrugations, is close to stagnant

---

[9] Appendix C, Eq. C.3 [2].

[10] Appendix C, Eq. C.4 [2].

as the velocity is very low. The boundary layer can further be argued to have been displaced above the corrugations as the tube acts with an effective diameter of $\sim$ D-e.

In cases p/e = 10 and 20 an interpretation of a boundary layer is more clear. There are still recirculation occurring close to the wake of the corrugation but it is seen that the boundary layer reattaches to the wall between ratio z/w = 0.5 and 0.25-0.5 respectively as the profiles resembles the parabolic profile seen in smooth tubes. This can be confirmed by Figures 7c and 7e where the skin friction (based on the mean wall shear stress) as function of the streamwise direction is shown. At the reattachment zones the value of the skin friction should be close to 0 which is seen to happen at z/p = 1 and 0.8 for p/e = 10 and 20 respectively. Note that the low skin friction in Figure 7a is due to the flow being close to stagnant between the corrugations and not due to a reattachment zone. Furthermore, dynamic formation and detachment of small circulation zones, close to the wake of the corrugation could be seen for cases p/e = 10 and 20.

The thermal boundary layer is visualized in Figure 6, where the temperature is plotted as function of the streamwise direction, for each simulation of rough tube design. The sudden variation of the contours between the corrugations is a result of the periodic boundary conditions in order to prevent build-up of enthalpy. Figure 6 shows similar trends as for the hydrodynamic boundary layer where the wall boundary layer is entirely disturbed in the case of p/e = 2.2. However for p/e = 10 the thermal boundary layer start to increase in thickness close to the next corrugation which increases the thermal resistance and results in a reduction in the enhanced heat transfer. For p/e = 20 the thickness of the boundary layer is increasing at z/w = 0.33, reducing the heat transfer before another corrugation is introduced. This is showed by Figures 7d and 7f where for p/e = 20 the heat transfer almost reduces to that of a smooth tube. It is thus further confirmed that the maximum heat transfer enhancement occurs for p/e close to 10 and that further increase of the ratio above 20 would yield increased heat transfer only in the vicinity after the corrugation. However in sense of operational cost the best option would be p/e = 2.2 as it in relation to 10 and 20 yields similar heat transfer enhancement but not as high pressure drop.

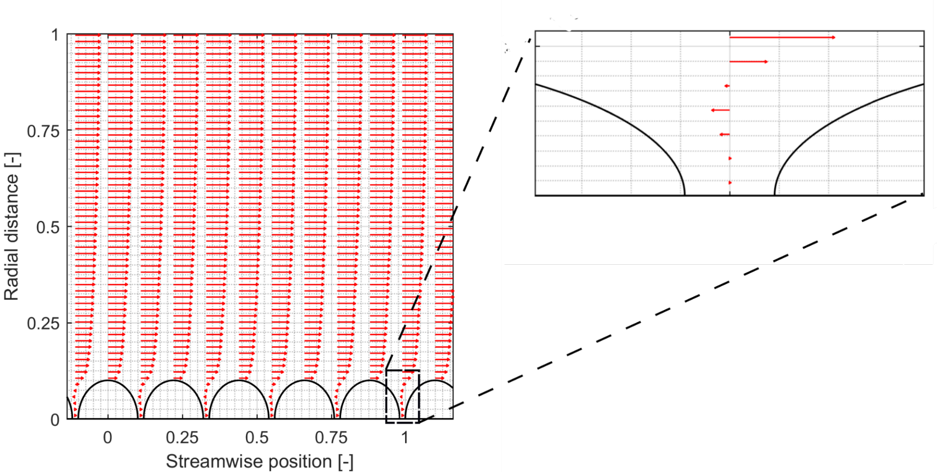

(a) p/e = 2.2

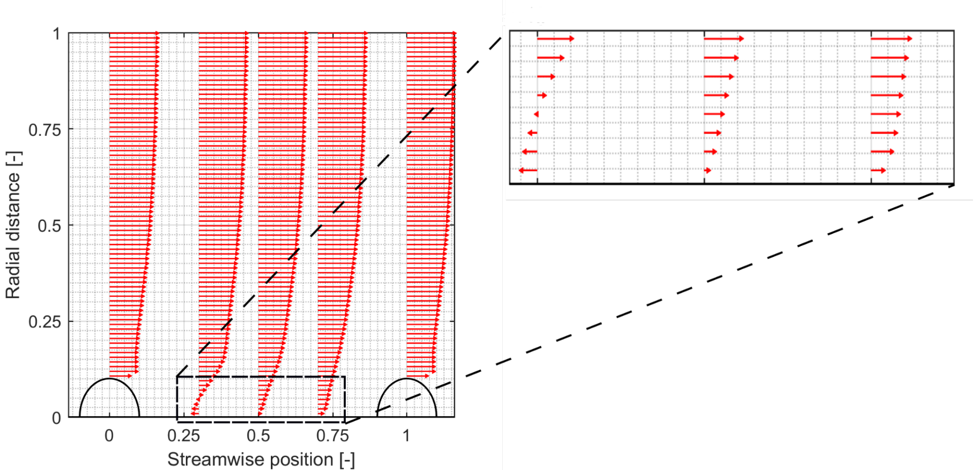

(b) p/e = 10

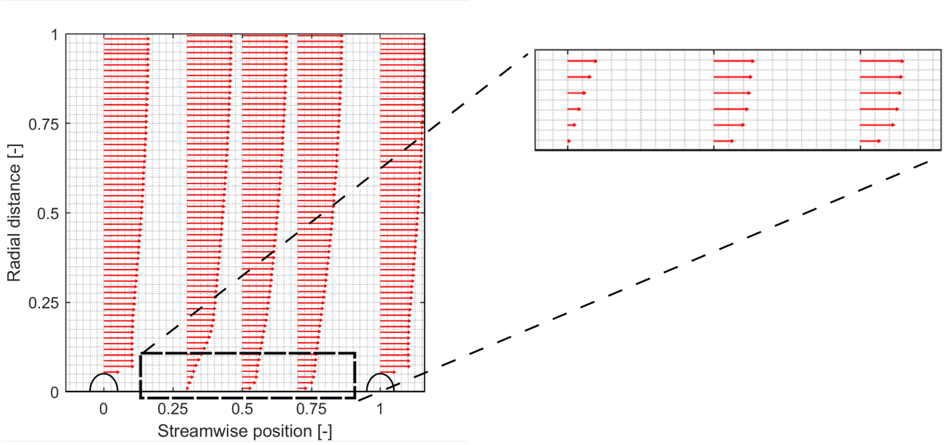

(c) p/e = 20

Figure 5: Streamwise velocity vectors from the wall into the center of the tube flow, for the simulations of different rough wall geometries.

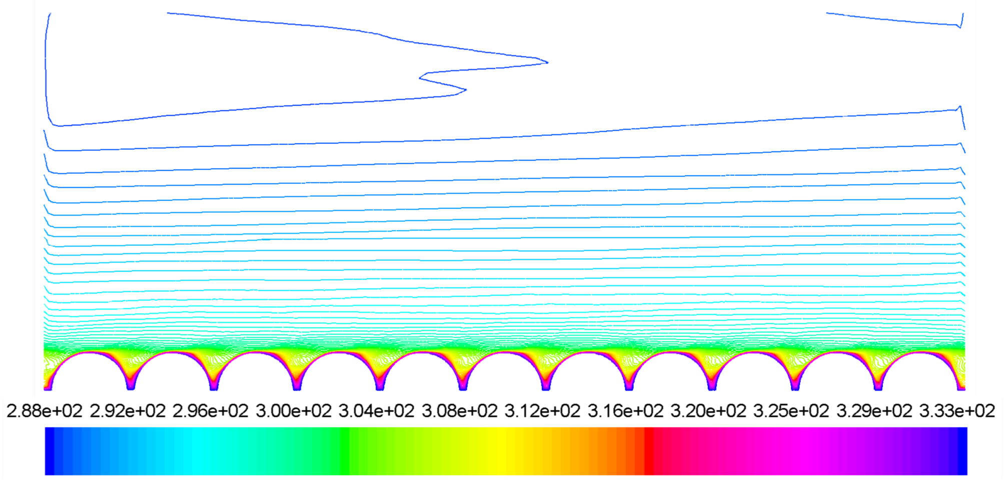

(a) p/e = 2.2

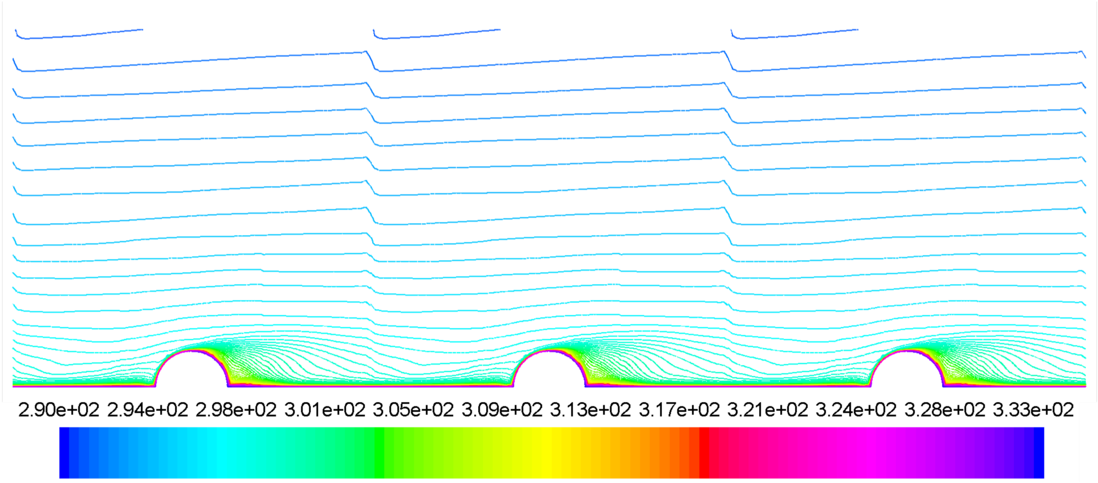

(b) p/e = 10

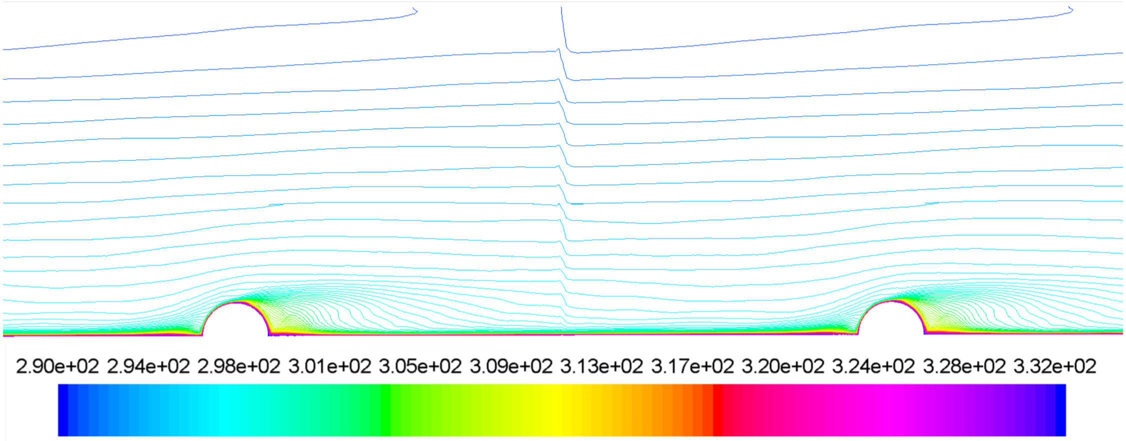

(c) p/e = 20

Figure 6: Contours over temperature in relation to the streamwise position for the roughness simulations.

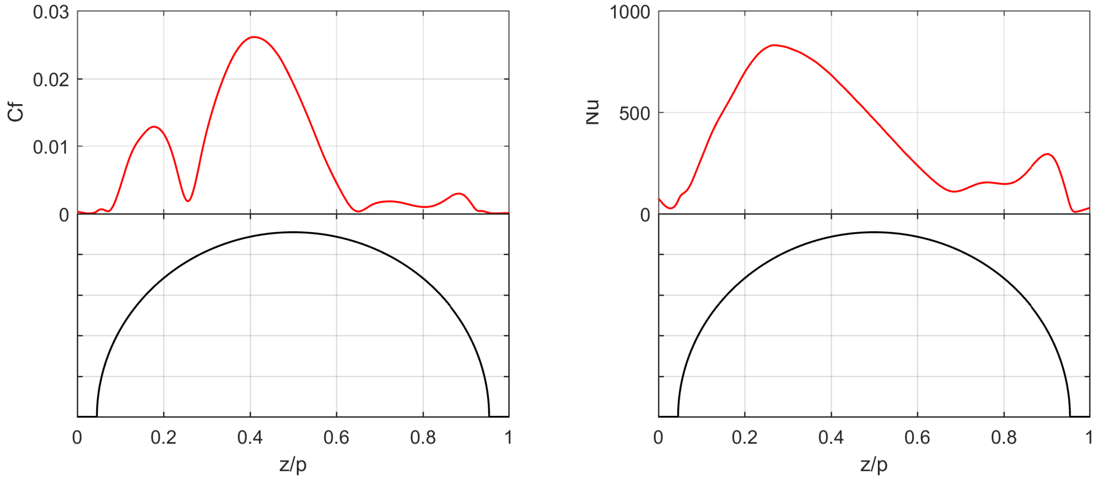

(a) Skin friction (C_f), p/e = 2.2 **(b)** Nusselt number, p/e = 2.2

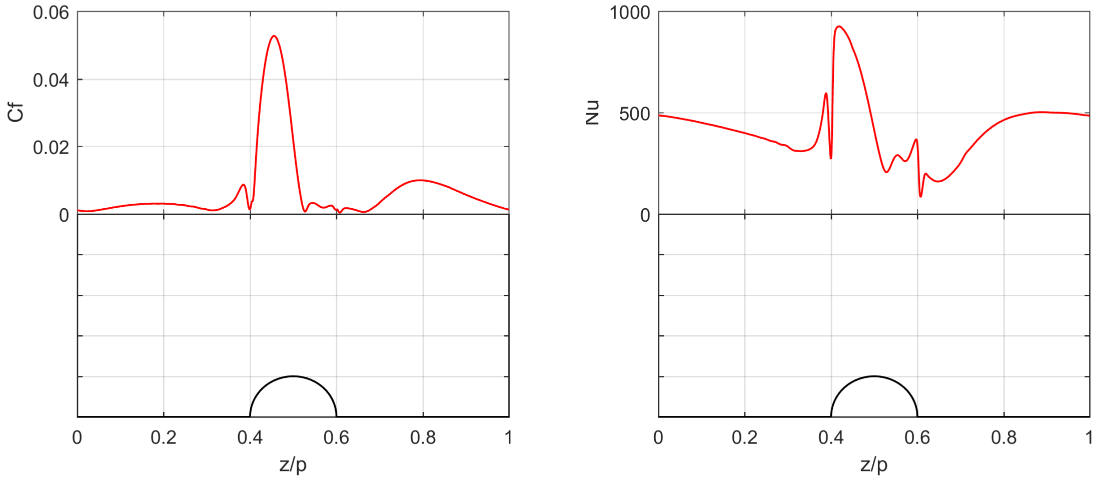

(c) Skin friction (C_f), p/e = 10 **(d)** Nusselt number, p/e = 10

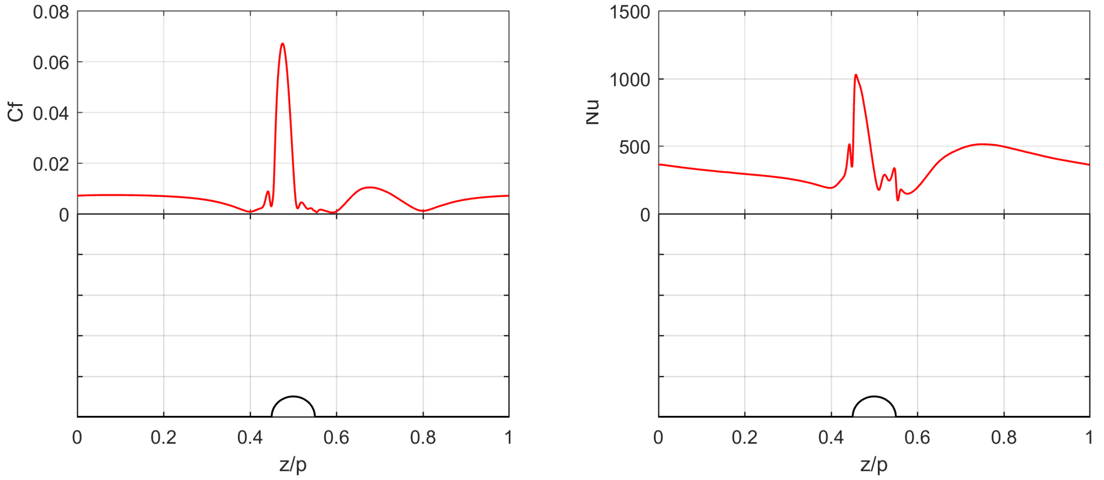

(e) Skin friction (C_f), p/e = 20 **(f)** Nusselt number, p/e = 20

Figure 7: Streamwise distribution of skin friction C_f and Nusselt number in relation to the position of the corrugation for respective rough wall simulations.

4.4 Dimensionless profiles

Figure 8 shows results from the LES simulations of smooth and rough wall geometries. Further compared to a rough wall function (Eq. 2.53) of the same roughness element height as in this study. The profiles are shifted downwards, as was expected. The downward shift for each rough wall simulation is approximately 7, 15 and 14 respectively. However it can be noted that the profiles for case p/e = 10 and 20 are shifted further down than p/e = 2.2 thus leading to believe that more parameters than k^+ and the type being important for proper wall function behavior. Not so unexpectedly, the pitch to roughness height ratio (p/e) seem to be an important parameter as these are shifted further down than p/e = 2.2. Furthermore the profile of p/e = 20 is shifted less downwards than p/e = 10, which is believed to be caused by the fact that if p/e would go towards infinity the profile would be the same as for the smooth tube, thus explaining the slightly upward shift. This is also in agreement with the pressure drop being lower for p/e = 20 than p/e = 10.

The rough wall function as stated in section 2.6.1, is dependent on the roughness height and the type of roughness, but also on roughness regime. As the sand-grain roughness (Eq. 2.53) is densely spaced it makes sense to only be comparable with the case of p/e = 2.2. The resulting dimensionless roughness height for p/e = 2.2, 10 and 20 were 102.5, 152.7 and 134.9 respective and thus falling under the fully rough regime. In that case the additive constant in Eq. 2.53 is 8.0. As seen in Figure 8 the data of p/e = 2.2 does not collapse onto the rough wall function, but instead indicate a similar shift between the wall function and the LES data as seen for the smooth case, which is believed to be due to the low Reynolds effect discussed earlier.

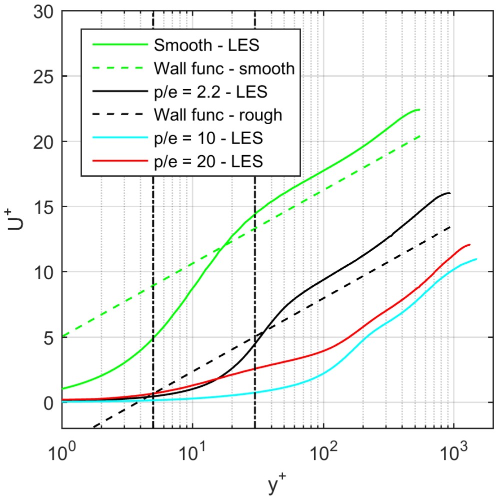

Figure 8: Dimensionless velocity profiles for LES Simulation of p/e = 2.2, 10 and 20 compared to smooth.

The dimensionless temperature profiles are shown in Figure 9 where p/e = 2.2, 10 and 20 are shifted by 25, 10 and ~9.5 respectively. The data of the smooth LES is in good agreement with Eq. 2.49 and a similar low Reynolds shift in the inertial subrange as the velocity profile is observed. It can be seen that cases p/e = 2.2 and 10 do not collapse on the inner wall function ($T^+ = Pr\ y^+$) which is most likely due to how the curves are shifted to the virtual origin. Points that are close to the wall are thus removed resulting in temperatures that are lower than the wall at the virtual origin leading to Eq. 2.51 being larger than 0 close to the wall. This is not the case for p/e = 20 because there is no virtual shift done as the mean velocity data is not zero except for at the wall.

The dimensionless temperature profile for p/e = 2.2, does not match with the wall function (Eqs. 2.55-2.56) taken from Kays and Crawford, [26] and Dipprey and Sabersky, [3]. In Eq. 2.55 the Stanton number (St_k) is determined from an empirical correlation for densely spaced spheres (Eq. 2.56) which is believed to be a reason for the large shift, as p/e = 2.2 is half-cylinders and separated by a small distance. However this difference was not seen for the velocity profiles.

The positions of the profiles are nearly the same as for the velocity profiles, however the p/e = 10 and 20 are above p/e = 2.2 which in sense could indicate that the temperature profile falls back to the smooth profile faster than the velocity profile as the distance between the corrugations is increased. This argument can be strengthened by viewing Figures 10 and 11 where the normalized[11] velocity and temperature profile are plotted at different streamwise positions after the corrugation. As shown the temperature profile indicate a faster return back to the smooth curve as the distance is increased. However caution should be taken when analysing the dimensionless temperature profiles, shown in Figure 9, as they are dependent on the post-processing of the data, which is not easily done as there is limited literature describing this. Furthermore the normalized raw data of Figure 11 is more easier understood as less tampering of the data is done. Though the main objective of the dimensionless profiles is to depict how the properties behave in order to yield better wall functions for rough wall problems which can be said to be achieved. However in terms of analysing the profiles and how it behaves in relation to the smooth curve, it is more advantageous to analyze the raw data.

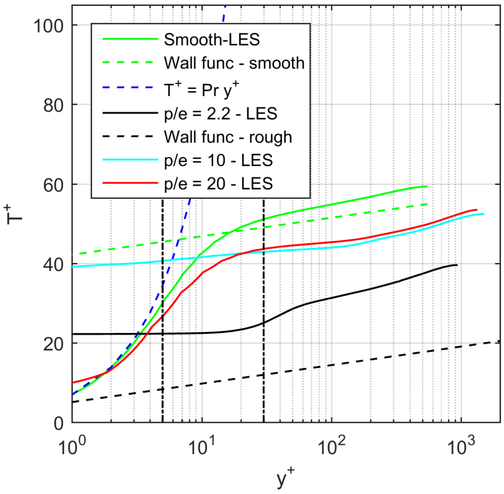

Figure 9: Temperature profiles for the smooth, p/e = 2.2, 10 and 20, compared with the smooth and rough wall function.

---

[11] Velocity is normalized by bulk velocity and temperature is normalized by the wall temperature

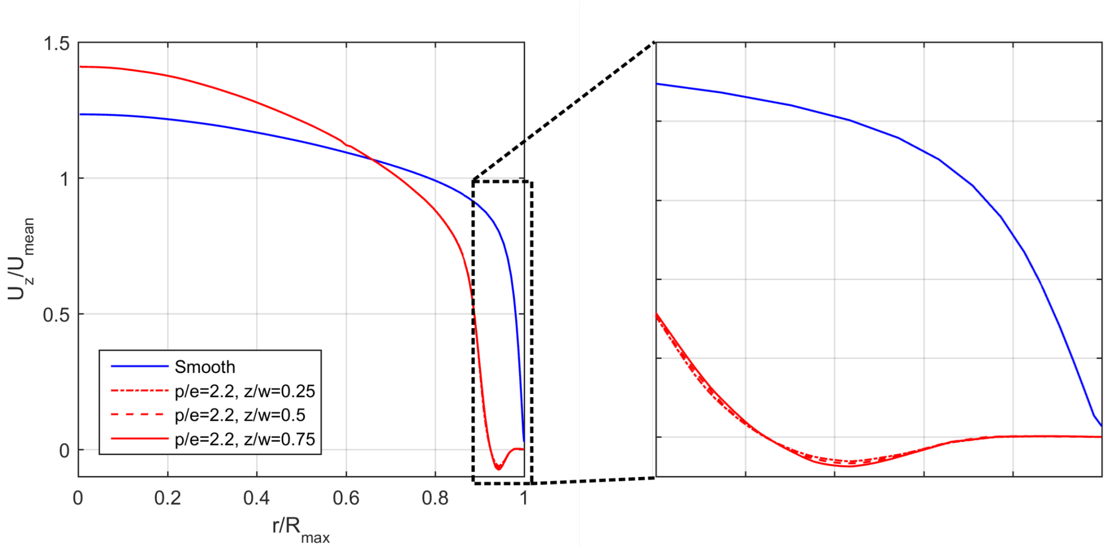

(a) p/e = 2.2

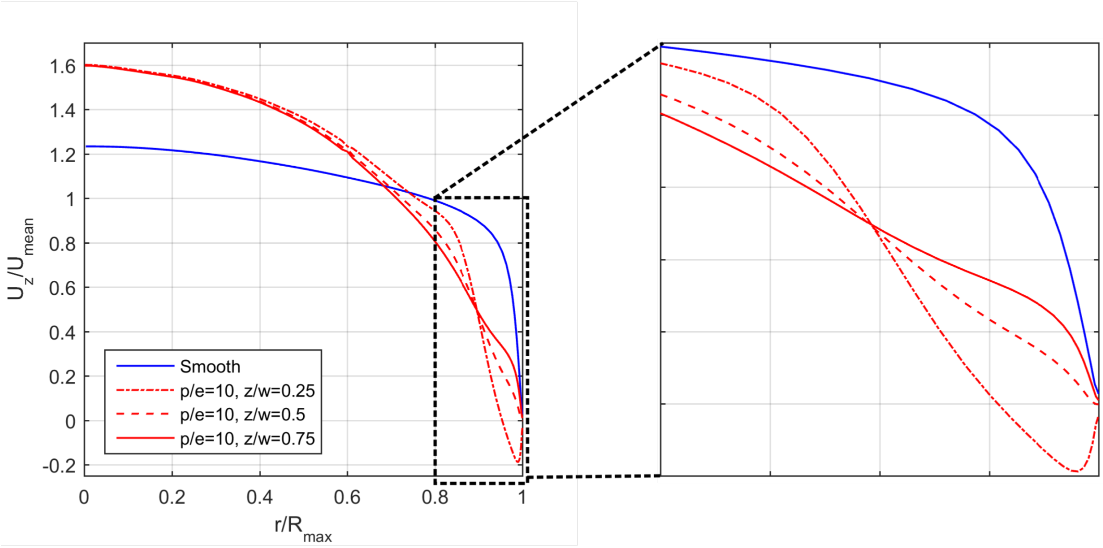

(b) p/e = 10

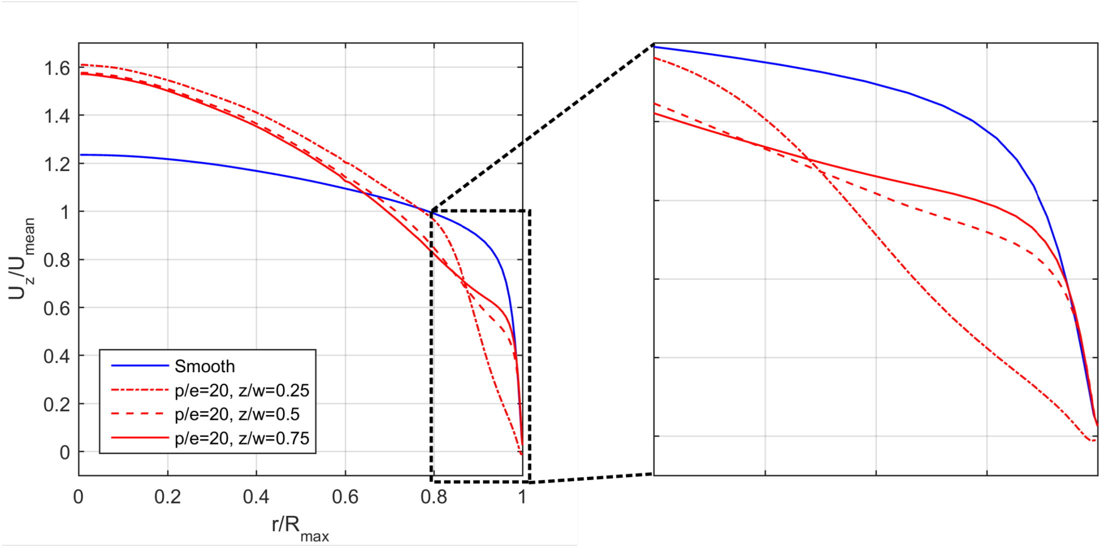

(c) p/e = 20

Figure 10: Normalized velocity profiles for all rough wall designs.

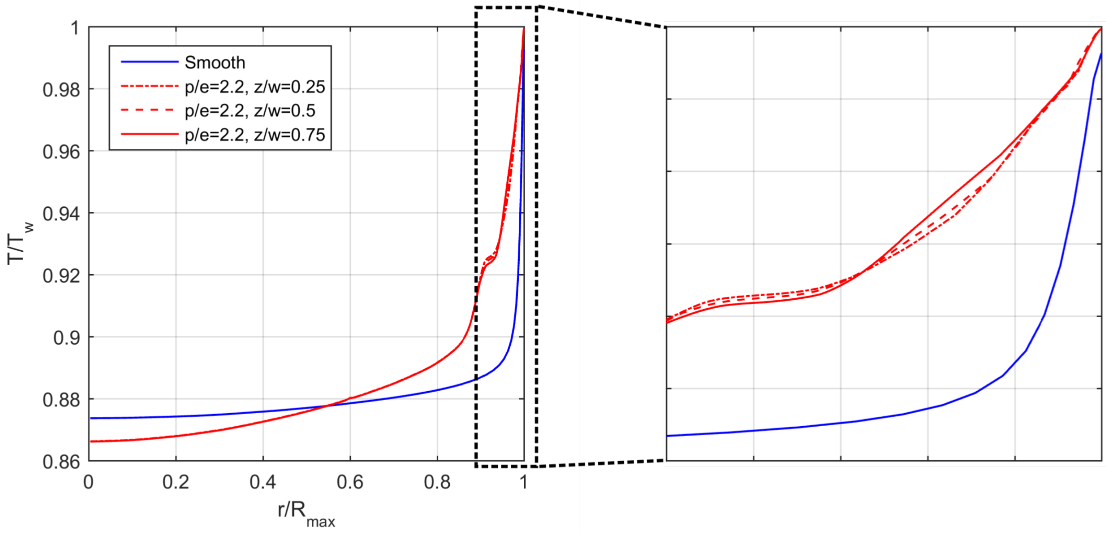

(a) p/e = 2.2

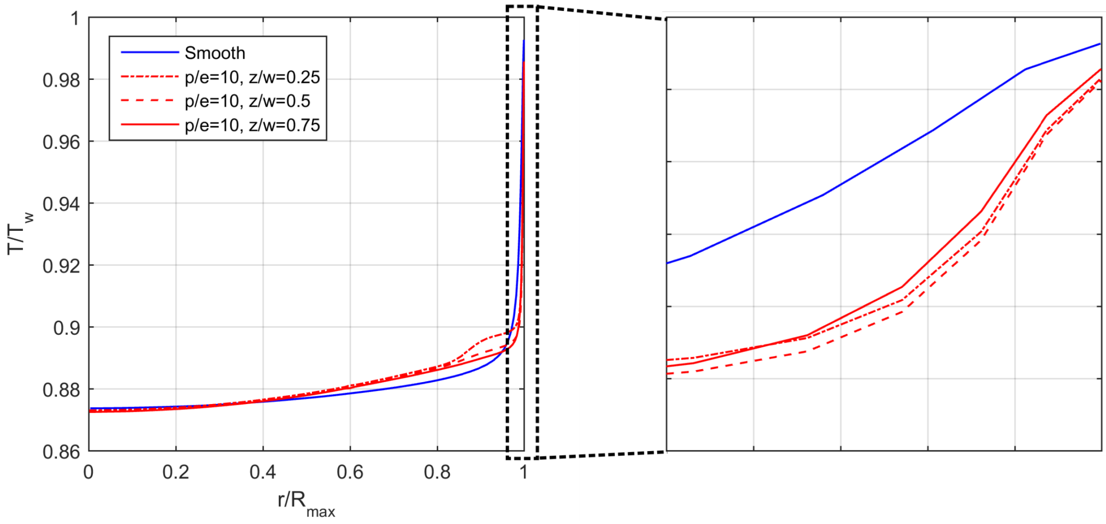

(b) p/e = 10

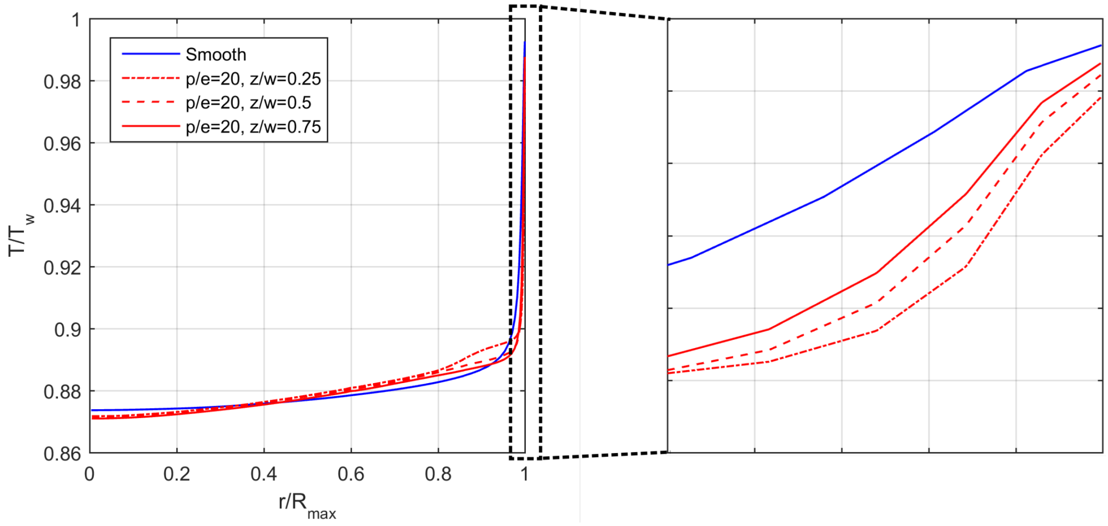

(c) p/e = 20

Figure 11: Normalized temperature profiles for all rough wall designs.

5 Conclusion

In this work heat transfer enhancement was investigated using LES simulations by introducing internal corrugations in a tube with internal diameter of 5 cm and flow characteristics of 20000 in Reynolds number. The simulations were performed on a smooth tube and three different roughness tubes where the pitch (p) to roughness height (e) ratio was varied from 2.2, 10 and 20 for the respective cases. For each simulation the heat and momentum transfer is quantified in the form of Nusselt number and pressure drop and compared to empirical correlations. The smooth tube and p/e = 2.2 case achieved good agreement with the correlations, whilst the agreement for case p/e = 10 and 20 were not as good, partly due to the lack of correlations.

The resulting heat transfer was enhanced for all the roughness simulations. It could be seen to have a maximum at p/e = 10 where the heat transfer was enhanced by around 220 %. The pressure drop also had its maximum at p/e = 10 which was increased by 662 %. p/e = 10 also enables most enhancement of heat transfer over the distance between the corrugations as the enhanced heat transfer started to decrease only prior to the next corrugation, compared to p/e = 20 where the boundary layer thickness starts to increase after one third of the distance between the corrugations and thus reducing the heat transfer. However in terms of operational costs the p/e = 2.2 case yields the highest heat transfer enhancement in relation to pressure drop as it yields a similar increase in heat transfer performance as p/e = 10 but has a pressure drop only a factor of 3.44 larger than the smooth case, instead of 7.62 as for p/e = 10.

It could be concluded that the "general" wall functions for the smooth and rough (densely packed) case is Reynolds dependant as the LES data does not collapse on the wall function. Furthermore the velocity and temperature profiles in the near wall region are strongly dependent on the separation of the corrugations, and further partly dependent on the post-processing method of how the shifting to the virtual origin is done.

5.1 Future investigations

Future aspects could be to use data from this study to present a formulation for wall function handling of corrugated tubes in flow and heat transfer problems. Creation of a more universal wall handling approach for roughness parameters would need further studies on different types of roughness and optimization of different geometrical parameters.

References

[1] Kuppan T. *Heat exchanger design handbook.* CRC Press, Boca Raton, 2nd edition, 2013.

[2] Welty James R, Wicks Charles E, and Wilson Robert E and Rorrer Gregory L. *Fundamentals of momentum, heat, and mass transfer.* Wiley, Chichester; Hoboken, N.J;, 5. edition, 2008.

[3] Dipprey D. F. and Sabersky R. H. Heat and momentum transfer in smooth and rough tubes at various prandtl numbers. *International Journal of Heat and Mass Transfer*, 6(5):329,IN1,333–332,IN1,353, 1963.

[4] Intergovermental Panel on Climate Change (IPCC). Climate Change 2014 Synthesis Report. `http://www.ipcc.ch/pdf/assessment-report/ar5/syr/AR5_SYR_FINAL_SPM.pdf`. Accessed: 2016-02-02.

[5] García A, Solano J. P, Vicente P. G and Viedma, A. The influence of artificial roughness shape on heat transfer enhancement: Corrugated tubes, dimpled tubes and wire coils. *Applied Thermal Engineering*, 35(1):196–201, 2012.

[6] Kathait PS and Patil AK. Thermo-hydraulic performance of a heat exchanger tube with discrete corrugations. *Applied Thermal Engineering*, 66(1-2):162–170, 2014.

[7] Webb R. L., Eckert E. R. G. and Goldstein R. J. Heat transfer and friction in tubes with repeated-rib roughness. *International Journal of Heat and Mass Transfer*, 14(4):601–617, 1971.

[8] Mirzaei M., Sohankar A., Davidson L. and Innings F. Large eddy simulation of the flow and heat transfer in a half-corrugated channel with various wave amplitudes. *International Journal of Heat and Mass Transfer*, 76:432–446, 2014.

[9] Lee Jae H., Sung Hyung J. and Krogstad Per-Åge. Direct numerical simulation of the turbulent boundary layer over a cube-roughened wall. *Journal of Fluid Mechanics*, 669:397–431, 2011.

[10] Krogstad P., Andersson H. I., Bakken O. M. and Ashrafian A. An experimental and numerical study of channel flow with rough walls. *Journal of Fluid Mechanics*, 530:327–352, 2005.

[11] Perry A. E., Schofield W. H. and Joubert P. N. Rough wall turbulent boundary layers. *Journal of Fluid Mechanics*, 37(2):383–413, 1969.

[12] Tennekes Hendrik and Lumley John L. *A first course in turbulence.* MIT Press, Cambridge, Mass, 1972.

[13] Andersson Bengt, Andersson Ronnie, Håkansson L, Mortensen M, Sudiyo,R and van Wachem, B. G. M. *Computational Fluid Dynamics for Engineers.* Cambridge University Press, Cambridge, 2011.

[14] Pope Stephen B. *Turbulent flows.* Cambridge University Press, Cambridge, 2000.

[15] Tritton D. J. *Physical fluid dynamics.* Clarendon, Oxford, 2. edition, 1988.

[16] Wilcox David C. *Turbulence modeling for CFD.* DCW Industries, La Cãnada, Calif, 3rd edition, 2006.

[17] Sagaut Pierre. *Large eddy simulation for incompressible flows: an introduction.* Springer, New York;Berlin;, 3rd;3. aufl.;3;third; edition, 2006;2005;.

[18] Smagorinsky J. General circulation experiments with the primitive equations: I. the basic experiment. *Monthly Weather Review*, 91(3):99–164, 1963.

[19] Nicoud F. and Ducros F. Subgrid-scale stress modelling based on the square of the velocity gradient tensor. *Flow, Turbulence and Combustion*, 62(3):183–200, 1999.

[20] Kim Won Wook and Menon Suresh. An unsteady incompressible navierstokes solver for large eddy simulation of turbulent flows. *International Journal for Numerical Methods in Fluids*, 31(6):983–1017, 1999.

[21] Menter F. R., Kuntz M. and Langtry R. Ten years of industrial experience with the sst turbulence model. begell, 2003.

[22] ANSYS, Inc. ANSYS Fluent Theory Guide Release 17.0, 2016.

[23] Patankar S. V., Liu C. H. and Sparrow E. M. Fully developed flow and heat transfer in ducts having streamwise-periodic variations of cross-sectional area. *Journal of Heat Transfer*, 99(2):180–186, 1977.

[24] Beale Steven B. Use of streamwise periodic boundary conditions for problems in heat and mass transfer. *Journal of Heat Transfer*, 129(4):601–605, 2007.

[25] Schlichting Hermann. *Boundary-layer theory.* McGraw-Hill, New York, 7. edition, 1979.

[26] Kays William M. and Crawford Michael E. *Convective heat and mass transfer.* McGraw-Hill, New York, 2. edition, 1980.

[27] Bredberg Jonas. On the Wall Boundary Conditions for Turbulence Models. *Internal Report 00/4*, 2000. *Department of Thermo and Fluid Dynamics*, Chalmers University of Technology, Gothenburg.

[28] Cebeci Tuncer and Bradshaw Peter. *Momentum transfer in boundary layers.* Hemisphere Publishing Corporation, New York, 1977.

[29] Tani Itiro. Drag reduction by riblet viewed as roughness problem. *Proceedings of the Japan Academy, Series B*, 64(2):21–24, 1988.

[30] Pimenta M. M., Moffat R. J. and Kays W. M. Structure of a boundary layer on a rough wall with blowing and heat transfer. *Journal of Heat Transfer*, 101(2):193–198, 1979.

[31] Cui Jie, Patel Virendra C. and Lin Ching-Long. Large-eddy simulation of turbulent flow in a channel with rib roughness. *International Journal of Heat and Fluid Flow*, 24(3):372–388, 2003.

[32] Nikuradse J. Stromnungsgesetz in rauhren rohren (english translation: Laws of flow in rough pipes). *vDI Forchunngshefte 361*, 1933. Tech. Rep. NACA

Technical Memorandum 1292. National Advisory Commission for Aeronautics, Washington, DC, USA (1965).

[33] Bhatti and Shah. *Turbulent and Transition Flow Convective Heat Transfer in Ducts.* Wiley, New York, 1987. Handbook of single-phase convective heat transfer, Kakaç, Sadk and Shah, R. K. and Aung,Win.

[34] T. S. Ravigururajan and A. E. Bergles. Development and verification of general correlations for pressure drop and heat transfer in single-phase turbulent flow in enhanced tubes. *Experimental Thermal and Fluid Science*, 13(1):55–70, 1996.

[35] Ghasempour Farideh. Structures, properties and dynamics of turbulent vortices, PhD Thesis, Chalmers University of Technology, 2015.

[36] El Khoury George K., Schlatter Philipp, Noorani Azad, Fischer Paul F., Brethouwer Geert and Johansson Arne V. Direct numerical simulation of turbulent pipe flow at moderately high reynolds numbers. *Flow, Turbulence and Combustion*, 91(3):475–495, 2013.

[37] Eggels J. G. M., Unger F., Weiss M. H., Westerweel J., Adrian R. J., Friedrich,R. and Nieuwstadt F. T. M. Fully developed turbulent pipe flow: a comparison between direct numerical simulation and experiment. *Journal of Fluid Mechanics*, 268(1):175–210, 1994.

[38] Okamoto Shiki, Seo Shozo, Nakaso Kouichirou and Kawai Itsurou. Turbulent shear flow and heat transfer over the repeated two-dimensional square ribs on ground plane. *Journal of Fluids Engineering, Transactions of the ASME*, 115(4):631–637, 1993.

Appendix A Geometries of each tube

Figure A.1 shows the geometries used in the different cases.

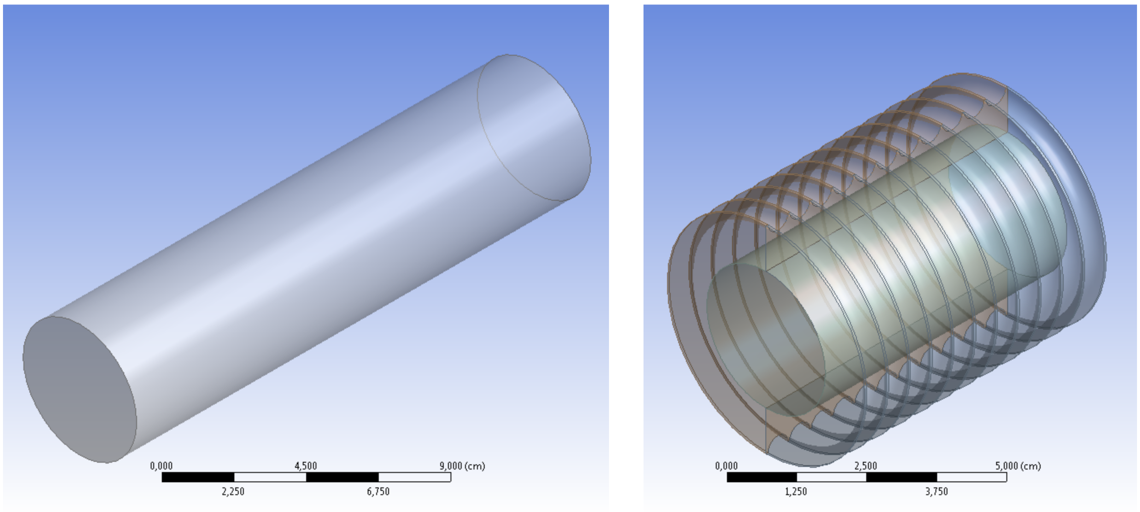

(a) Smooth **(b)** Rough - p/e = 2.2

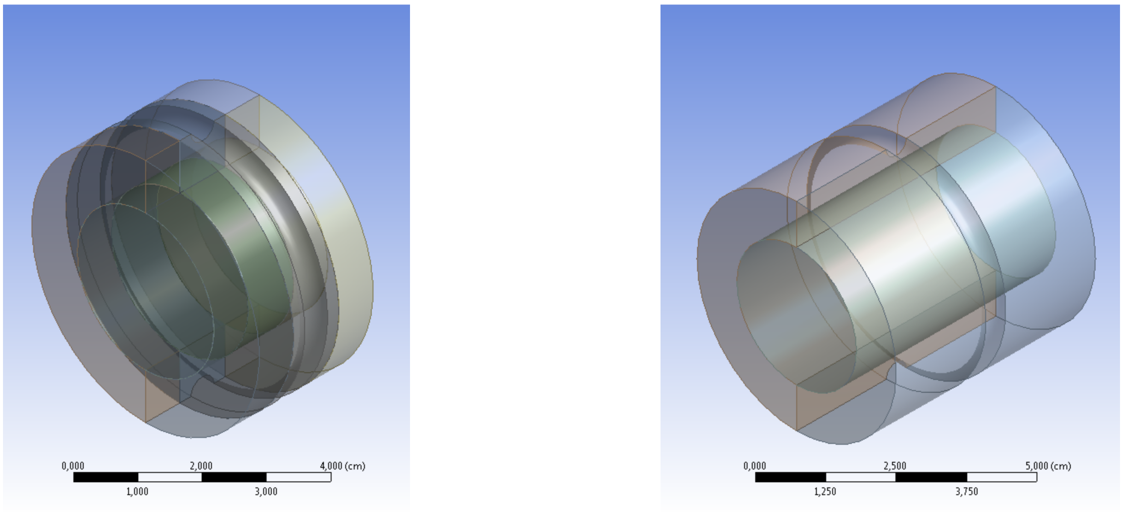

(c) Rough - p/e = 10 **(d)** Rough - p/e = 20

Figure A.1: Geometries of the different simulations performed.

Appendix B Initialization of simulation for RANS models

Initialization of the flow, turbulent and thermal quantities needs to be done. The example below demonstrates the typical procedure of estimating initialization values.

The streamwise velocities (z) is calculated from the expected Reynolds number of 20000 and the diameter of the pipe:

$$u_z = \frac{Re\ \nu}{D} = \frac{20000 \cdot 1e^{-6}}{5e^{-2}} = 0.4\ [m/s]$$

Whereas the velocities in the spanwise directions were assumed to be negligible in magnitude in comparison of the streamwise velocity and thus initialized as zero.

The turbulent quantities were calculated assuming that these quantities could be taken from large anisotropic eddies which would then give the turbulent quantities necessary for the initialization as:

$$k = u_{fluct}^2 = 0.0025\ [m^2/s^2]$$

and

$$\omega = \frac{\varepsilon}{k} \approx 14\ [1/s]$$

where k is the turbulent kinetic energy, u_{fluct} is the velocity fluctuations assumed to be ∼10 % of the streamwise velocity, ω is the specific dissipation rate and epsilon is the turbulent dissipation calculated from:

$$\varepsilon = \frac{k^{3/2}}{l} \approx 0.036\ [m^2/s^3]$$

where l is the length scale of the larger eddies defined as $l = 0.07\ D \approx 0.046\ m$

Appendix C Correlations

$$\frac{1}{\sqrt{f_{smooth}}} = 4.06\ log_{10} Re \sqrt{f_{smooth}} - 0.60, \tag{C.1}$$

$$\frac{1}{\sqrt{f_{rough}}} = 4.06\ log_{10} \frac{D}{e} + 2.16. \tag{C.2}$$

Where f is the Fanning friction factor for smooth and rough respectively and $\frac{D}{e}$ is the diameter to roughness height ratio.

$$Nu_{smooth} = 0.023\ Re^{0.8}\ Pr^{0.4} \tag{C.3}$$

$$Nu_{rough} = \frac{Re\ Pr\ (f_{rough}/2)}{1 + \sqrt{(f_{rough}/2)}(4.5\ Re_e^{0.2}\ Pr^{0.5} - 8.48)} \tag{C.4}$$

where Re_e is the roughness Reynolds number based on the roughness height ($Re_e = \epsilon u_* / \nu$).

$$(2/f)^{0.5} = 2.5\ log(D/(2e)) - 3.75 + 0.95\ (p/e)^{0.53} \tag{C.5}$$

$$\begin{gathered} f_{rough}/f_{smooth} = \Bigg(1 + \Big[29.1\ Re^{(0.67-0.06\,p/D-0.49\,\beta/90)} \cdot \\ (e/D)^{(1.37-0.157\,p/D)} \cdot\ (p/D)^{(-16.6e^{-6}\ Re-0.33\,\beta/90)} \cdot \\ (\beta/90)^{(4.59+4.11e^{-6}\ Re-0.15\,p/D)}\ \cdot \\ (1+2.94/n_{corners})\ sin(\beta_{rib})\Big]^{15/16}\Bigg)^{16/15} \end{gathered} \tag{C.6}$$

Where β is the helix angle relative to the tube axis, set to 90°and β_{rib} is the profile contact angle of the rib to the internal surface also set to 90°. $n_{corners}$ is the number of sharp corners of the rib, which is set to a high number to signify a smooth circular surface.